AALBORG UNIVERSITY
STUDENT REPORT

# Biodistribution of Polymer-Drug Conjugates *in vivo*

Master Thesis for the Master Course Nanobiotechnology


Student: Piotr Ziemczonek
Study no.: 20171762

assessor: Leonid Gurevich, Ph.D


10 September 2019

I would like to dedicate this work to my parents, who always pushed me to cross my limits, and to my sister, without whom I would have never decided to study abroad. Thank you for having faith in me.

Special thanks to Dr. Leonid Gurevich for supervising this work.

I want to thank Dr. Sam Moré for the opportunity to conduct my study in his company, DendroPharm. Colleagues from the company are also being thanked, Monika and Markus, for the time spent on talking about the more and less science-related topics. Special thanks go to Michael for sharing his knowledge and experience in the times of doubts.

My friends from Berlin, Marek and Iwona, are thanked for taking care of me and reminding that this thesis is not the only thing in the world to think of.

My friends from Warsaw, Robert, Maciek and Darek, thank you for supporting me despite the distance that divides us.

Dziękuję!

# Abbreviations

| | |
|---|---|
| **AAG** | $\alpha_1$-acid glycoprotein |
| **ADME** | absorption, distribution, metabolism and excretion |
| **API** | active pharmacological ingredient |
| **ASBT** | apical sodium dependent bile acid transporter |
| **AUC** | area under curve |
| **BBB** | blood-brain barrier |
| **BCRP** | breast cancer related protein |
| **CL** | clearance |
| **CLSM** | Confocal Laser Scanning Microscope |
| **CNS** | central nervous system |
| **Cy3** | Cyanine 3 |
| **DF** | degree of functionalization |
| **DMSO** | dimethyl sulfoxide |
| **EPR** | enhanced permeation and retention effect |
| **F** | bioavailability |
| **FITC** | fluorescein-5-isothiocyanate |
| **FPE** | first pass effect |
| **GFP** | green fluorescence protein |
| **HD** | hydrodynamic diameter |
| **hPG** | hyperbranched polyglycerol |
| **HPMA** | N-(2-hydroxylopropyl)-methacrylamide |
| **HSA** | albumin |
| **i.v.** | intravenous |
| **LCST** | lower critical solution temperature |

| | |
|---|---|
| **MCT1** | monocarboxylic acid transporter 1 |
| **MDRI** | multidrug resistance transporter 1 |
| **MPS** | mononuclear phagocyte system |
| **MRP2** | multidrug resistance associated protein 2 |
| **MW** | molecular weight |
| **NIR** | near infrared |
| **OATP** | organic anion transporting polypeptide |
| **PD** | pharmacodynamics |
| **PEG** | polyethylene glycol |
| **PEPT1** | peptide transporter 1 |
| **PG** | propylene glycol |
| **PK** | pharmacokinetics |
| **PNIPAAM** | Poly(N-isopropylacrylamide) |
| **PPB** | plasma protein binding |
| **QD** | Quantum dots |
| **s.c.** | subcutaneous |
| **t ½** | half-life |
| **Vd** | volume of distribution |

# Table of content

# 1. Introduction

## 1.1 Biodistribution of Xenobiotics

During the studies on a new drug to be introduced on the market, there is a need to know how the body will react to it. In other words, what is the organism going to do with the xenobiotic (a foreign substance), from the moment of administration until it is eliminated from the organism. In pharmacology, a branch that studies those transitions is called pharmacokinetics (PK). It analyzes the metabolic changes of the substance and its fate from the moment of administration to the point, when it is completely eliminated from the organism. Another important information comes with the knowledge of pharmacodynamics (PD) of the compound, which studies the correlation between the concentration of the entity at the place of action (where receptors, enzymes or transporters are present) and the pharmacological response. However, information obtained from both of the above can vary in dependence on the experimental conditions, as well as on species, age and/or gender [1].

Once the drug enters the body, it will go through several phases until gets eliminated. Those phases are abbreviated as ADME, which refers to absorption, distribution, metabolism and excretion. For most of orally administered compounds (p.o.), thy have to reach the intestinal lumen before it gets absorbed. Prior to entering the systemic circulation, it is delivered to the liver and exposed to Phase I metabolism (and/or) biliary excretion (the process called first pass effect - FPE). A dose of the drug administered intravenously (i.v.) does not undergo FPE, as it is already introduced to venous circulation. It may however get eliminated through the lungs in expired air or get metabolised prior to entering the arterial circulation. With the arterial blood, the entity will be distributed within the organs and tissues. Some of them, like kidney can metabolise and excrete it alongside the liver. Therefore the availability of the active compound in the concentration facilitating the therapeutic or toxic effect is influenced by those processes and transitions [2].

Apart from p.o. and i.v., there are several other routes of drug administration: dermal, subcutaneous (s.c.) - in the cutaneous tissue, intranasal (i.n.) - into nasal epithelium, and intraperitoneal (i.p.) - into the body cavity. Regardless of the route of administration, the compounds have to transpass the membrane prior to being absorbed. Since the p.o.

administration is the most common way of drug administration, the GI tract is the first important site of absorption. If administered as a solid, the dose should dissolve before reaching the intestinal membrane. To increase the dissolution rate one can slightly increase the temperature, lower the particle size (therefore increase surface area/volume ratio) or alter the pH if the compound is prone to protonation or deprotonation, however extreme pH can cause tissue irritation or the precipitation of the compound after administration. Altering the solution composition by introducing non-aqueous co-solvents is also possible in preclinical studies. This includes ethanol, propylene glycol (PG), polyethylene glycol (PEG) 300, dimethyl sulfoxide (DMSO) and solubilizing agents, like β-cyclodextrin [3]. The last one should be used with an awareness, as it tends to bind strongly to some of the compounds and therefore results in inefficient release after i.v. administration. Charman et. al. have reported that a cyclodextrin-based formulation of ozonide antimalarial resulted in a ca. 8-fold decrease in the blood volume distribution and a ca. 7-fold decrease in the average residence time, when compared to the isotonic glucose-based formulation [4]. The content of co-solvents should yet be lower than 20% of the injection volume due to the possible hemolysis, enzymes inhibition and/or toxic effects. Permeation of the membrane however depends on molecular weight (MW), lipophilicity and charge of the particle. Due to the high hydrophobicity of the membrane, the compound should also have a sufficient lipophilicity in order to passively diffuse on the other side of the membrane. The lipophilicity of the compound and compound-membrane interaction can be assessed by calculation $\log_P$ (partition coefficient), which is a ratio of concentration of the un-ionized compound in two immiscible solvents, 1-octanol (organic) and water, at equilibrium. For ionizable compounds, $\log_D$ (the distribution coefficient) is an appropriate indicator, as it is calculated from the ratio of ionized and unionized entity in organic (1-octanol) and aqueous (buffer, pH = 7.4) solvents. $\log_D$ values of -0.5 and 2 are believed to be optimal for oral administration. Compounds with values below this range exhibit poor membrane permeability, while the ones with values higher than 2 are poorly aqueous-soluble.

The size also plays a role, as the entities with MW < 200 and high water-solubility can travel paracellularly through the junctions between the enterocytes. Compounds with higher MW are more likely to pass transcelluraly in active or passive transport. There are several uptake transporters in the luminal membrane of intestine, eg. OATP (organic anion transporting polypeptide) family, peptide transporter 1 (PEPT1), the apical sodium dependent bile acid transporter (ASBT), the monocarboxylic acid transporter 1 (MCT1). In contrast however, there are also ATP-dependent efflux transporters, multidrug resistance transporter 1 (MDRI), the

multidrug resistance associated protein 2 (MRP2) and the breast cancer related protein (BCRP), which play a role in active removal of the xenobiotic from the cell against a concentration gradient and since they are mostly present in the intestine and liver, they can significantly limit the bioavailability of the active substance after oral administration [5]. Also, if protonable, non-protonated form of the drug is more prone to transpass the membrane.

The blood-brain barrier (BBB) protects the central nervous system (CNS) from the external environment. It restricts the permeability for the hydrophilic entities, proteins with low molecular weight and charged molecules. It consists of a layer of endothelial cells, which are connected by tight junctions. Those junctions are 100 times more firm than in any other capillary endothelium and surround the whole margin of brain capillaries. The transport across the barrier can thus be facilitated transcellulary. In this manner the barrier is similar to the continuous cell membrane and reflects its behaviour in the context of the transport of substances [6]. It is permeable for small lipophilic substances, while large proteins and hydrophilic compounds transpass the BBB by the active transport, however it requires the presence of the ligand for the transporter [7].

Once entered the circulation, the compound will be distributed between the organs and tissues and the rate of distribution will depend on the ability of passively crossing the membrane and whether the compound is a substrate for active or efflux transporters as well as plasma protein binding (PPB).

Among plasma proteins (albumin (HSA), $\alpha_1$-acid glycoprotein (AAG), lipoproteins and α-, β- and γ -globulins), albumin and AAG play a major role in binding the xenobiotics [8]. Albumin has several hydrophobic binding sites and has a predominant affinity to bind organic anions (carboxylic acids and phenols), however it also binds drugs which are basic or neutral. It is also the most abundant of all plasma proteins (ca. 4% w/v of blood weight and 60% of all plasma proteins). Its physiological role is to maintain the blood pH and osmotic pressure, as well as to transport molecules [9]. AAG however, is present in plasma to much smaller extent (<0.1 % w/v) and has only one binding site per molecule, yet it binds drugs via nonspecific interactions and exhibits higher binding affinity compared to albumin, primarily to basic compounds, but it also binds hydrophobic entities, like steroids. The primary function of AAG is to transport steroids through the body. The binding rate depends upon the concentration of the compound and proteins and can differ between the species. It has been reported that unbound fraction of zamifenacin (muscarinic antagonist) was 20-fold lower (0.01 %) in humans when compared to rat (0.2%) and 10-fold lower when compared to dog (0.1%) [10].

Elimination mostly occurs by metabolic changes which alter the lipophilic xenobiotic entity into more hydrophilic metabolites to further excrete them with bile or urine. Most of the xenobiotic metabolism occurs in the liver, however other organs, as well as intestinal microflora play a role in the breakdown of the compound. The metabolism of xenobiotics can be split into Phase I and Phase II reactions. Reactions of Phase I is an addition of a functional group, eg. hydroxyl, amine, carboxylic group due to reaction of oxidation, reduction and hydrolysis. In humans, Phase I is facilitated by the CYP1, CYP2 and CYP3 families of cytochrome P450 superfamily. Over 2000 of those hemethiolate enzymes have been identified up to date and they are believed to be responsible for around 90% of all xenobiotic metabolism. They appear as membrane proteins located either in the inner membrane of mitochondria or in the endoplasmic reticulum, mostly in hepatocytes. They contain a heme group with Fe atom in the center. During the catalytic cycle (Figure 1), the binding of the substrate with the enzyme changes the conformation of the active site of an enzyme and induces the electron transfer from NADPH. Subsequently, molecular oxygen binds to the ferrous heme center giving rise to a dioxygen adduct. After second electron transfer, the adduct is reduced to an unstable peroxo state, which is quickly protonated, releasing a water molecule. Remained intermediate (Compound I) is a major oxidizing agent. It abstracts the hydrogen from the substrate to further transfer the hydroxyl group onto the same substrate, at the same restoring the enzyme complex to the resting (initial) state [11].

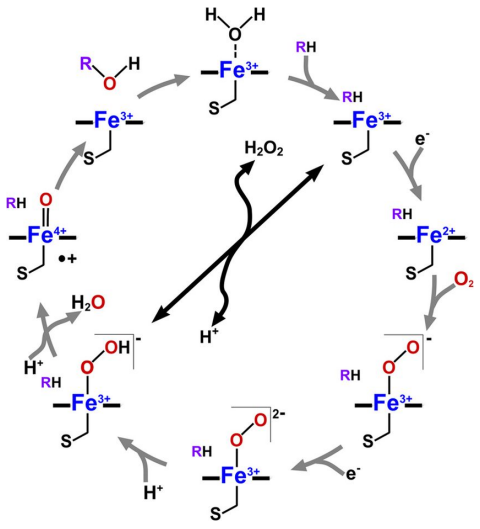


Figure 1:Schematic illustration of a CYP mediated metabolism of a xenobiotic. Taken from: [12]

The major fraction of metabolising processes occur in the liver, however other organs (kidney, placenta, skin, intestine) also contain all necessary enzymes and therefore have an ability to metabolise the xenobiotic entity.

Phase II of the metabolism of xenobiotics involves enzymes - transferases, which are involved in reacting of the metabolite with charged, high-molecular weight entities, such as glutathione, sulfate, glycine, or glucuronic acid. Obtained products are highly polar and have increased MW, therefore are unable to passively diffuse through the cell membrane. Due to that fact, efflux transporters like breast cancer resistance protein (BCRP) and multidrug resistance proteins (MRPs) are used to transport the metabolised entities. Furthermore, the Phase II enzymes are usually located at the same site as the mentioned efflux transporters [13].

### 1.1.1. Assessment of availability

The assessment of the compound disposition *in vivo* can be performed by the characterization of four factors: clearance (CL), volume of distribution (Vd), half-life (t ½) and bioavailability (F). CL is a measure of the ability of the organism to eliminate the xenobiotic within time. There are two major ways of elimination to remove the compound out of the body is as mentioned, metabolism (as it decreases a compound concentrations due to enzymatic breakdown) and excretion, but information of clearance rate does not serve to identify the route of elimination. It does however provide vital information regarding the duration of drug efficacy and calculating the concentration of the drug in the body.

Clearance rate can be calculated for the elimination of the compound from the whole body (systemic clearance) or for the particular organs (organ clearance). Since the liver and kidneys play a major role in the xenobiotic elimination, knowledge on clearance thereof can provide useful information on the impact of the drug-drug interaction or current disease state on this process.

The volume of distribution is expressed in volume units, however it is a proportional coefficient between the total drug amount administered and the concentration of the drug in the body fluids (eg. plasma) at a given time. If the compound is strongly bound to plasma, $V_d$ will not change over time, and will approximately reflect the total plasma volume. If, however, the compound is further distributed within organs, $V_d$ will change overtime until reaching an equilibrium.

The drugs half-life gives is a measure of the time after which the concentration of the compound in the measured tissue (eg. plasma) is equal to 50% of initial concentration. Yet this value may differ among species. Smaller
species (eg. rat) with faster metabolism will eliminate the the compound quicker than bigger ones (eg. human) and since distribution is a rapid process, t ½ is governed by its elimination.

The bioavailability is a fraction of the measured substance that reaches the systemic circulation after administration and is provided for the administration route other than i.v. , because of the loss of the compound after the intake, mostly to poor absorption from the GIT (p.o. administration), or enzymatic breakdown of the active substance. Therefore to correctly determine all parameters, they should be measured after an i.v. administration, because the whole amount of the measured compound is systemically available. The bioavailability of the compound can be estimated from the area under curve (AUC) which reflects the total exposure of the body to the compound, if one knows the initial dose of the drug administered [2].

### 1.1.2. Models for PK estimation

To simplify the estimation of the PK of a substance, compartmental and non-compartmental analysis can be performed. In the compartmental approach it is assumed that the organism is made of compartments which are connected and interact with each other. A compartment is a tissue or an organ (or set of organs), which is kinetically uniform. The simplest model treats the organism as one compartment, where the drug is distributed evenly and has equal concentration in every fluid and tissue. In this unicompartmental model the drug's concentration in fluids and tissues is reflected by the blood plasma concentration and assumes that the metabolism and excretion thereof is directly proportional to the concentration in the body. Not all tissues, however, have the same blood supply. Due to this fact the drug is distributed faster in the organs and tissues with better blood supply, like kidney and liver, and will enter and leave slower from the organs and tissues with a lower blood flow, for example fat tissue. If one takes into account those relations and rate of elimination from those two groups of tissues (with bigger and smaller blood supply), then an organism is considered as made of two-compartment model. The central compartment is the one, where the drug distribution is more rapid due to good blood supply, whereas the peripheral compartment represents organs

and tissues with lower blood flow.

Non-compartmental analysis uses AUC for calculating the pharmacokinetics of the compound. As mentioned above, it reflects an overall exposure of the body to the compound, as its plasma concentration over time. The AUC is estimated using linear or logarithmic trapezoidal methods for calculating AUC over two adjacent time points. However, both of them are prone to some errors, therefore the help comes from commercially available software, which use a combination of both. AUC is plotted as the compound concentration over time from 0 to infinity. It is generally useful when comparing several formulations with the same dosage (eg. capsule vs. tablette) to assess whether the same amount of drug is absorbed and enters the systemic circulation. AUC is also used for monitoring the drugs with a narrow therapeutic window (small range of compounds's dosage, within which the compound acts effectively without causing toxic effects). For example, warfarin is an anticoagulant drug for treating deep vein thrombosis and preventing the patients with atrial fibrillation or valvular heart disease from stroke, but when its present in the body in too high concentrations, then is can cause internal bleeding [14].

### 1.1.3. Allometric scaling

Once data from the experimental *in vivo* analysis is obtained, it is possible to predict the pharmacokinetics of a compound in humans. This process is called allometric scaling. The empirical observations proved that some of the physiological processes are a function of size and weight. Therefore most of the anatomical variables can be scaled up using equation $Y = aW^b$, where *Y* is a physiological parameter (eg. volume of distribution), *W* is the animal weight, *a* is the allometric coefficient and *b* is the allometric exponent. Knowing the PK value from the other species, it is possible to predict the value of this parameter in humans, according to equation $Y_{human} = Y_{animal} (W_{human}/W_{animal})^b$

Already in the '80s, Mordenti J. successfully proved this correlation by collecting the data of half-life of 12 antibiotics in different animals (mice, rats, rabbits, monkeys and dogs) and using this data to predict the half-life of those drugs in humans with a weight of 70 kg. His results confirmed the connection between the animal size and the drug's half-life, however due to some deviations, it was pointed out that this correlation should be considered as a helpful tool

for making such predictions, as the pattern of behaviour was observed, but it should not be taken as a biological law. Moreover, he denoted that biological processes in different species take different amounts of time when referring to the relative concept of time (seconds, minutes, hours etc.), however they occur in equivalent ‘portions’ of time, when speaking of the biological clock (expressed in heartbeats in a life span), which is illustrated in Figure 2 [15].

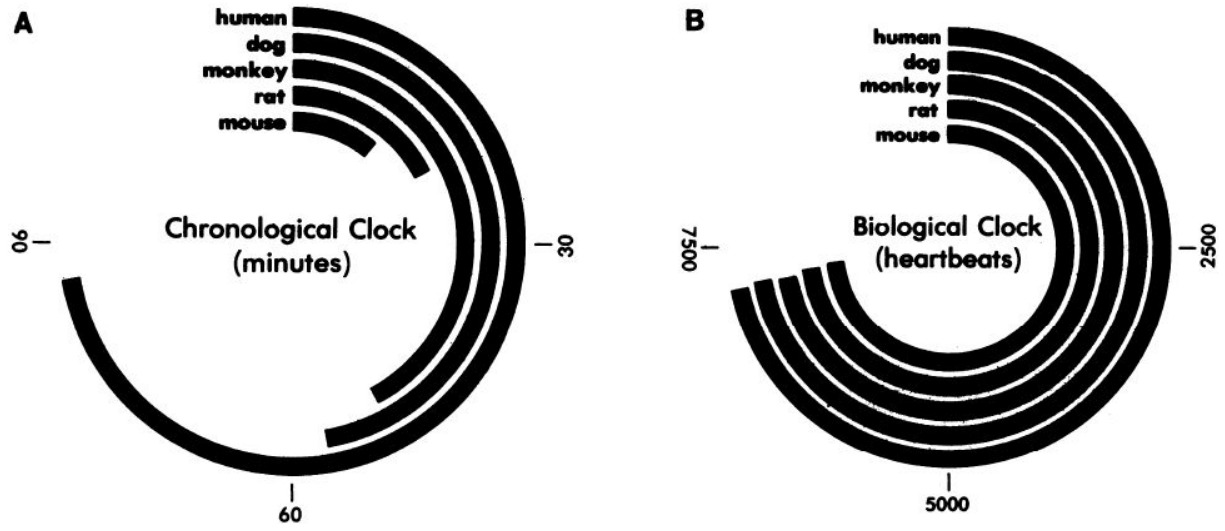


Figure 2: Illustration of the concept of a life span in regard to the relative time (A) vs. biological clock (B). It suggests that considering the number of physiological processes in the body (for example the number of heartbeats), most of the mammals live the same equivalent of those. Taken from: [15]

### 1.1.4. Clearance of high MW molecules

Once a nanomaterial enters the bloodstream, it is taken up by the organs. The main site of accumulation is the mononuclear phagocyte system (MPS). Depending on the charge and size, the particles can undergo the opsonization and adsorption by the serum proteins. This effect can enhance the recognition by the immune system of the host, but also will result in the increase of the hydrodynamic diameter (HD), which is essential when it comes to the clearance of the molecule [16]. The effective pore size of the endothelial layer of the blood vessels is approx. 5 nm, thus the particles with a HD < 5 nm will establish the equilibrium with the extracellular extravascular space faster when compared to bigger constructs. Lymphatic vessels exhibit similar structure, however the endothelial layer thereof is a little more permeable, with the pore size of 6 nm [17].

Ideally the nanomedicine, after fulfilling the therapeutic action, should be effectively eliminated from the body and should not aggregate in the organs. However, it is stated that biomedical agents tend to stay within the organs for an extended period of time, mostly due to the non-specific uptake by the MPS, which can later make the biodegradation and further excretion much harder. The remaining entities can lead to toxic side effects in the host organism [17].

Up to date, it has been noticed that MPS organs (liver and spleen), are the main site of destination for nanomedical agents [18]. The reason for that behaviour is believed to lie in the discontinuous, fenestrated capillaries. Similar effect of increased permeability has been observed in sites of inflammation and tumors, due to the rapidly growing vascular structures. This phenomenon is called an enhanced permeation and retention effect (EPR) and is recently being used for passive targeting [19].

It has been also stated, that size plays an important role in the time of blood circulation and extravasation, as particles with size smaller than 5 nm are excreted by the renal clearance, whereas the particles within range of 10-20 nm will be rapidly taken up by the liver. The particles with the size over 200 nm are going to be filtered by sinusoidal spleen or recognized and

digested by the MPS [16]. Spleen, as a part of MPS, plays an important role in the metabolism of xenobiotics. It acts as a blood reservoir, but its major function is to filter the blood. It consists of white pulp, responsible for the production of T- and B-lymphocytes, and the red pulp, which mechanically filters blood, but also holds a reservoir for over a half of the body's monocytes [20]. It is known that the splenic filtration is observed for particles that exceed the size of 200 nm. Alternatively, the nanoparticles can be phagocytosed by macrophages present in the red pulp [21].

Liver is the main organ responsible for the metabolism and clearance of most of the xenobiotic agents. It consists of parenchymal (hepatocytes), non-parenchymal (Kupffer cells) cells and intrahepatic lymphocytes, which participate in the elimination of the foreign entity. Hepatocytes and Kupffer cells are facilitating the two major elimination pathways, which are strongly size dependent. The particles with size ~200 nm are effectively taken up by Kupffer cells due to the slow blood flow in the sinusoids, which allows the efficient phagocytosis and macropinocytosis. The hepatic sinusoid endothelium has fenestrations with a diameter of approximately 100-200 nm, therefore particles with smaller size can enter into the Disse space and enter the lymphatic circulation or can be taken up by the hepatocytes and enter the billary excretion pathway [22]. It was documented that 20 nm polystyrene nanoparticles were found in hepatocytes and subsequently observed in the bile, which indicates the possibility of this route of elimination [23]. It is also be examined, that opsonization via plasma proteins enhances the uptake by Kupffer cells due to the large number of receptors for those proteins, but also because the increased overall size of the aggregates [24]. One of the most common approaches to improve the PK of the nanoparticles is PEG-gylation, which is binding the polyethylene glycol chans on the surface of the particle. This results with reduced immunogenicity and elongated half-life, distribution and increased elimination [25].

Renal clearance is a preferable pathway of nanoparticles elimination. The process consists of glomerular filtration and tubular secretion and reabsorption. The glomerulus is made of three interacting layers: a fenestrated endothelium with fenestrations of 80-100 nm in diameter, the glomerular basement membrane with 200-400 nm of thickness and the slit diaphragm built of the podocytes with 5 nm in pore size between the podocytes. The negatively charged proteoglycans present in the endothelium, together with the different pore size of the glomerular layers creates the size- and charge-selective barrier [26]. It has been reported that QDs with zwitterionic cysteine coating were effectively eliminated with the urine when the particle size was below 5.5 nm. Particles with higher size did not undergo renal excretion. It

should be noted that *in vivo* the size and charge of the nanoparticle can be altered due to protein absorption, affecting the surface charge and hydrodynamic radius. In this case, the elimination pathway will likely be shifted to the liver. It has been reported that positively charged molecules are renally excreted to the biggest extent (due to interaction with fixed negative charges in the endothelium), while anionic molecules are the least readily filtered [27].
However, is has been reported that particles with ~75 nm in diameter are prone to accumulate in clusters within mesangial cells and induce toxic effect [28].

## 1.2. Fluorescence Analytical Techniques

### 1.2.1. Theory of Fluorescence and Working Principle of Fluorescence Microscopy

Fluorescence microscopy is an optical microscopy used in biological sciences for the examination of organic and inorganic substances, but the mode of detection is based on fluorescence or phosphorescence. Both terms refer to the emission of light upon excitation of the molecule in the singlet state, which was first described and published by a polish physicist, Aleksander Jabłoński in 1933.

The Jabłoński diagram (Figure 3) is an illustration of the electronic transitions upon photon absorption. Electrons are paired in their singlet state. It means that their spins are opposite. After absorption of a photon, the molecule can be excited from the ground state ($S_0$) to the first ($S_1$) or second ($S_2$) excited state. Each state possess several vibrational levels. Energy dissipation occurs via internal conversion, which is a non-radiative process of relaxation from higher vibrational level to lower vibrational level of an excited state. The molecule returns to the ground state by the emission of a photon with energy equal to the energy difference between $S_1$ and $S_0$. Fluorescence emission occurs within $10^{-8}$s, from the lowest vibrational level of $S_1$ state, because the internal conversion happens in $10^{-12}$s, therefore it is complete before emission of

the photon. However, upon fluorescence, the electron usually returns to the higher vibrational level of the ground state, and then relaxes to the lowest vibrational level of $S_0$.

In some cases, the electron can change the spin and go to the triplet state ($T_1$), where the paired electrons have the same spin. Photon emission from the triplet state is called phosphorescence and results in the emission of a photon with a longer wavelength (lower energy) compared to fluorescence. Transition from $S_1$ to $T_1$ is called intersystem crossing and it is a spin-forbidden process, which is why it occurs with the several orders of magnitude lower rate. Molecules containing heavy atoms (e.g. bromine, iodine) enhance the phosphorescence, as they facilitate intersystem crossing [29].

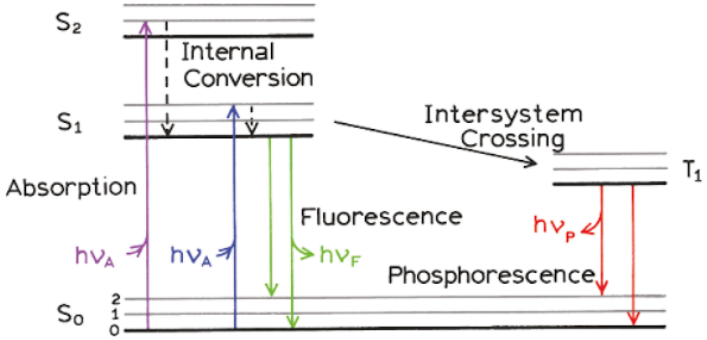


Figure 3: Jabłoński diagram, showing electronic transitions between the vibrational states of different excited singlet states ($S_1$ and $S_2$) and the intercrossing system from singlet to triplet ($T_1$) excited state. Taken from: [29]

During the examination of the specimen, it is illuminated by the light of a given wavelength, specified for a particular fluorophore. Upon excitation, the fluorophore emits the light with a longer wavelength (i.e. lower energy), which is then detected (Figure 4).

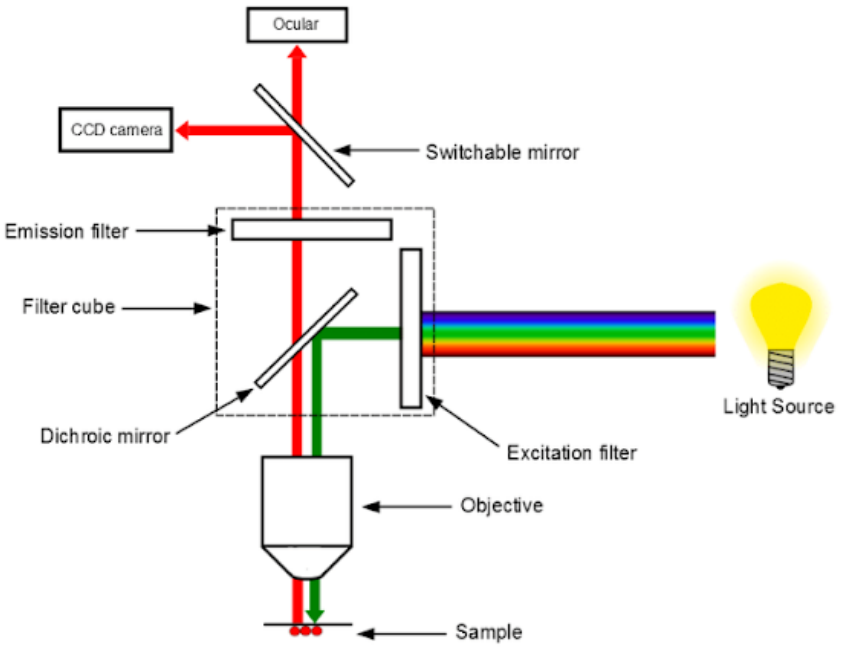


Figure 4: A schematic presentation of an epi-fluorescence microscope. The excitation light travels through the excitation filter, which lets pass only the desired wavelength. Upon excitation, the fluorophore emits the light, which is not absorbed by the dichroic mirror, but instead reaches the detector. The emission filter blocks any other wavelength but the emitted one. Taken from [30]

A conventional fluorescence microscope consists of a light source, the excitation filter, dichroic mirror and the emission filter. The light source requires high power, therefore it can be mercury-vapour lamp, the xenon arc lamp or high-power LEDs or lasers in more advanced setups. The emitted light goes subsequently through the excitation filter, where only the desired wavelength can travel through. The dichroic mirror directs the light towards the sample through an objective. Most of the microscopes used in biological sciences are epi-fluorescent (or incident light fluorescent), where the reflected fluorescent light travels back to the dichroic filter through the same objective. This filter allows only the emitted light wavelength to reach the detector, while the excitation light is absorbed. This strategy of illumination is advantageous, firstly, because the dichroic filter acts selectively for the light's wavelength and allows only the desired wavelength to reach the specimen. It also stops the remaining excitation light from reaching the detector (some fraction of the excitation light can, however, pass through the dichroic mirror, therefore the emission filter is mounted right before the detector to lower the background noise coming from the unwanted excitation light) . Secondly, the objective acts as a condenser for the excitation light reaching the specimen, but also the emission light is gathered

and forwarded to the detector. Because the emission light travels in the exactly opposite direction to the excitation light, the light scattered by the specimen is much less likely to travel back through the objective.Moreover, utilization of the same objective for both light pathways ensures that the objective is always in the right position regarding the luminescence of the specimen, since the site of the sample being observed is the one being illuminated. Finally, both light beams traveling through one objective can use the full numerical aperture (NA) thereof (NA is a constant describing the range of angles of light able to pass through the objective), yielding high-resolution images [31] .

### 1.2.2. Confocal microscopy

Unlike in conventional wide-field microscopy, in confocal microscopy, the light travels through a special pinhole to illuminate the smallest point possible. The obtained image is extended and appears as a blurry spot, due to the signal coming non-focused part of the specimen. To eliminate the blur, another pinhole is placed on the detector side, which has the same focus as the first pinhole (i.e. they are confocal with each other). Such arrangement eliminates out-of-focus signal and focuses the exciting light on only one point of the focal plane of the specimen, resulting in a better resolution when compared to the wide-field approach. Moreover, this setup allows to obtain better resolution in the depth direction of the specimen. By eliminating the background fluorescence of unfocused parts of the sample, also three-dimensional pictures are achievable (Figure 5). This requires the scanning over the regular pattern in the specimen. The thickness of the focal plane is described as the wavelength of the exciting light over the numerical aperture of the objective lens. [32]

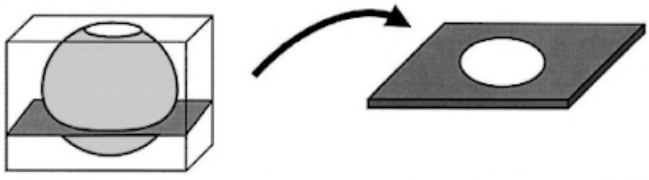

Figure 5: Optical sectioning of the sample. By eliminating the out-of-focus signal, it is possible to obtain the sections of the specimen in depth. Using the dedicated software, the sections can subsequently be piled up resulting in a 3D image of the examined specimen. Taken from [33]

The excitation sources commonly used in confocal microscopy are argon (Ar; 488 nm and 514 nm) and krypton (Kr; 568 nm) lasers (CLSM - Confocal Laser Scanning Microscope), however some set-ups include a mercury lamp, which provides the full range of wavelengths. In the latter approach, for scanning a specimen, a so-called Nipkow disk is used. A Nipkow disk is a black disk with several thousand apertures aligned in Archimedian spirals (Scanning Disk Confocal Microscope). While CLSM uses a single light spot to illuminate the specimen and scanning mirrors to scan the sample, in a Scanning Disk Microscope, the specimen is scanned with thousands of light spots simultaneously , capturing the image at video rate [34]. Confocal microscopy allows to capture images of living cells *in vivo*, as bigger depth into specimen is achieved, without the need of sectioning them before examination. This was a driving force behind the development of such a microscope by Marvin Minsky in 1955.

The applications of confocal microscopy include immuno- and fluorochrome staining, studies on gene expression and cellular trafficking, studying organelles with organelle-specific probes [33]. The technique is also harnessed as a diagnostic tool for determining the cornea thickness. It has been used for the *in vivo* examination of corneal nerve morphology at 700x magnification in diabetic patients. The technique was proven to be useful in assessing the nerve regeneration upon topical drug administration [35].

Although confocal microscopy is advantageous over conventional fluorescent microscopy, there are several drawbacks as well. Main of these is a limited range of available wavelengths due to laser light source. Also, if not suitably attenuated, the laser beam intensity can be harmful for living cells. This can however, be overcome by two-photon excitation [33].

### 1.2.3. Two-photon microscopy

Two-photon absorption is a process in which 2 photons arrive at the molecule ‘at the same time’ (i. e. within 0.5 fs), their energies sum up to value needed to promotion of the molecule (fluorophore) to the excited state. The dissipation of the energy (fluorescence) then

follows the normal emission pathway. Because this type of excitation is extremely rare, to increase the probability of such an event to occur, special femtosecond lasers are used, which emit ultrashort pulses with high frequency. Typically used lasers produce pulses 100 fs long with frequency of 10 MHz [35].

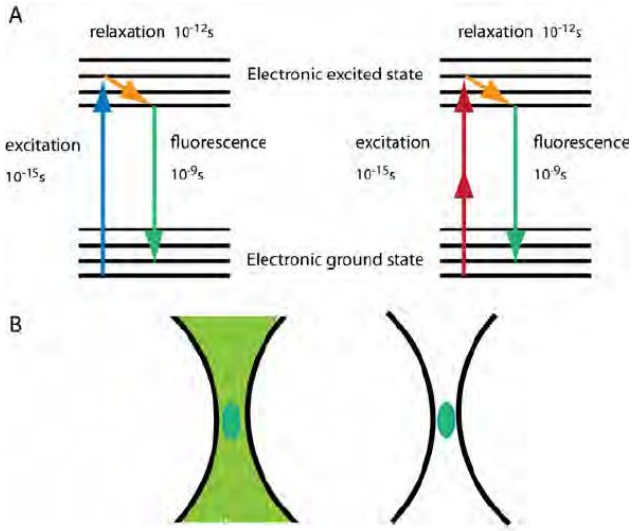


Figure 6: (A) comparison of one photon (left) vs. two photon (right) fluorescence. Unlike in one-photon fluorescence, two photons exciting the sample have shorter (red shifted) wavelength than the emitted photon. (B) Comparison of fluorescence signal concentration in two photon (right) vs one photon (left) excitation. The signal from two photon excitation is limited to focal plane, because the probability of this event depends quadratically on the photon density. Taken from [36]

The commonly used fluorophores absorb light of a wavelength of 400-500 nm. The laser used in two-photon microscopy operates in NIR (near-infrared) range (800-1000 nm). Thus, this type of excitation results with the emission peak of a shorter wavelength than the excitation wavelength (Figure 6A). Also, because the signal obtained depends quadratically on the photon density, two-photon absorption is limited to only the focal plane, eliminating the out-of-focus signal (Figure 6B). Also, the volume being excited at one time is ~1 fl, so there is no need for using the pinhole aperture for eliminating the noise. NIR wavelengths penetrate deeper parts of a tissue (> 500 um) and cause low phototoxicity, as there is no endogenous one-photon absorbers of this wavelengths in most tissues [37].

Therefore two-photon microscopy is widely used for *in vivo* imaging of living structures and processes in real time. The research group of Podgorski et. al. observed the rearrangement of neuron networks and single neuron structures during learning process in *Xenopus laevis* tadpoles. Using the two photon imaging for tracing somatic calcium transients, they observed

that upon a visual stimuli, over time the neural network forms a highly connected clusters of similarly responding network [38].

Another group of Park et. al. developed a new probe for two proton excitation, which is a derivative of 2-methoxy-6-(5-oxazolyl)naphthalene (fluorophore) and pyridine (protonation site). Upon protonation the probe changes the emission wavelength from blue towards green range. This probe was successfully used to measure the pH in living cells as well as stomachs of patients suffering from nonerosive reflux disease [39].

### 1.2.4. Spectrofluorimetry

Spectrofluorimetry allows for quantitative analysis of a fluorescent sample upon radiation with a specific wavelength. Since the fluorescence emission is directly proportional to the incident light, this method serves as a sensitive analytical tool and is mostly limited by the ability to detect a low intensity light. In contrast, the measurement of absorption relies on the ability to distinguish the incident light from the transmitted light.

A schematic illustration of the spectrofluorometer is shown in Figure 7.

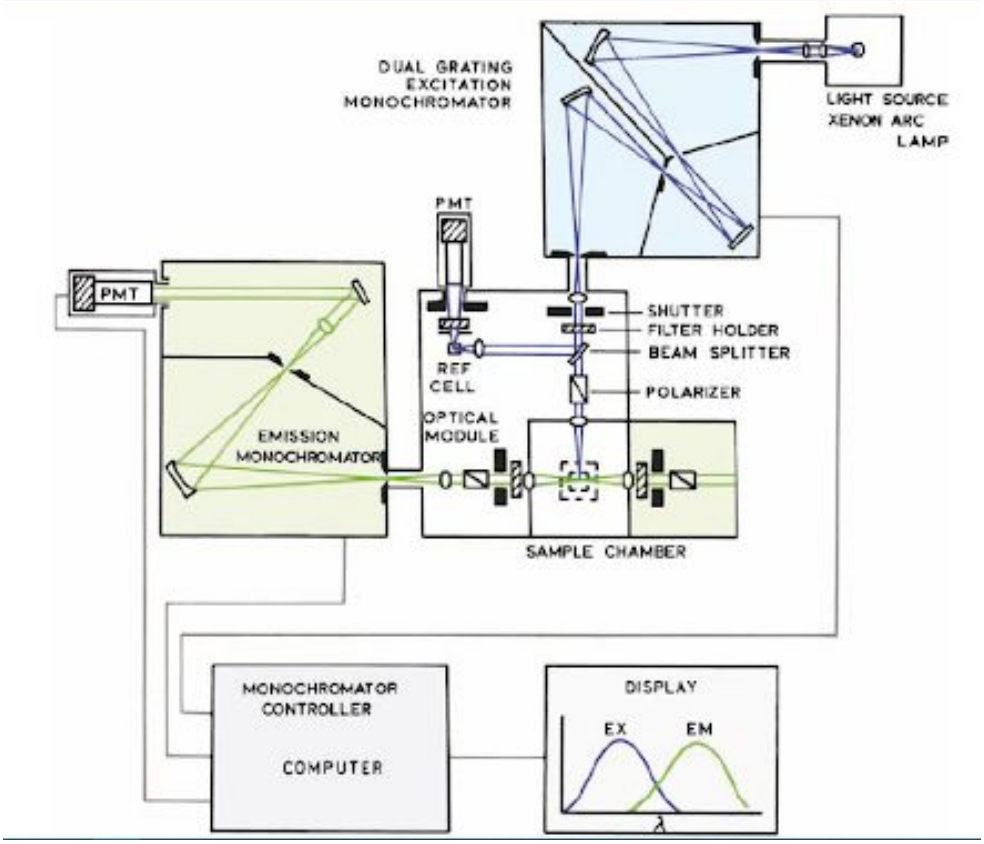


Figure 7: Schematic illustration of the spectrofluorometer. Taken from: [29]

The spectrofluorometer consists of a light source which emits light from UV to visible range of wavelengths. Usually xenon lamps are used, because high intensity of light is available at any wavelength within the produced range. The light passes through a monochromator, which mechanically splits the white light into various wavelengths, while preventing unwanted, stray light from hitting the sample. Set-up proposed in this Image contains also a monochromator for the emission wavelength. The shutters are used to exclude the excitation light and therefore prevent the sample from photobleaching or decomposition. The emission signal reaches the photomultiplier tubes, where it is detected. Appropriate software is used to quantify the amount of light detected. The beam splitter reflects a small fraction of incident light to the reference cell which is used for the correction of the light source intensity changes [29]. The detector is usually placed at a 90° angle from the excitation light, to lower the contribution of the transmitted stray light (light leakage) to the detected signal, as only stray light scattered by

the sample reaches the detector. Therefore the signal-to-noise ratio is lowered compared to the set up, where the detector is placed at 180° [40].

Data collected in the spectrofluorometer may be distorted by several reasons, like turbid, highly absorbing solutions, solvent fluorescence, light leakage, Rayleigh or Raman scattering. Rayleigh scattering refers to the scattered photons with the same wavelength as incident, whereas Raman scattering refers to scattering of the photons with different (usually longer) wavelength. This phenomenon is due to the virtual excited state induced by the incident light, where the electron is excited to higher vibrational level [41].

The intensity of emission is directly proportional to the concentration of the fluorophore and can be calculated, if the extinction coefficient is known. Otherwise, a series of standard solutions with known concentration can be measured to plot the calibration curve, which can be used as a reference.

### 1.2.5. Fluorescent labelling

There are multiple approaches to prepare the sample that is suitable for examination in the fluorescent microscopy. One can study the autofluorescence of the compartment built within the specimen, like chlorophyll, collagen and fluorite. Also, some drugs show autofluorescence eg. tetracycline [42]. This feature, however, enables only a narrow range of the substances to be examined. To extend the scope of researched particles and tissues, fluorescent labelling comes into play. The labelling probe has to meet certain requirements to be successfully applicable. It should be easily excitable and detectable via conventional equipment. The excitation, however should not induce the excitation of biological compartments of the sample. Moreover, it is supposed to give high signal, which refers to high molar absorption coefficient (i.e. it should absorb the light instead of scatter it or let it through) and high quantum yield (i.e. high number of photons emitted upon the previous absorption). It should also be thermally stable and soluble in the medium that is used in a particular study.

Early classes of fluorescent dyes include organic substances, like cyanines, fluoresceins and rhodamines, but also proteins, like GFP (green fluorescence protein). Organic dyes are advantageous with their low cost and availability, they are also easy to handle. On the other

hand, they exhibit short Stokes shift. They also have poorer photochemical stability and are more prone to photobleaching (decrease in signal emission due to the degradation), when compared to inorganic dye, which because of the advancement of material science, are believed to soon outperform the classic labels [43].

#### 1.2.5.1. Fluorescein dyes

Fluorescein dyes belong to ones widely used for labelling proteins. FITC (fluorescein-5-isothiocyanate) exhibits excitation maximum at 494 nm and is therefore chosen preferably in confocal microscopy and flow cytometry, as this wavelength lays close to 488 nm, which is a spectral line of the argon-ion laser. Yet, FITC (green fluorescence) is prone to photobleaching and exhibit lower sensitivity in the pH lower than 7. In contrast, rhodamine dyes (red fluorescence), like succinimidyl ester of 5-carboxyrhodamine 6G shows not only better photostability, but also possess longer wavelength emission maxima [44]. The excitation peak lays at 520 nm, close to 514 nm spectral line of the argon-ion laser, which makes rhodamine dyes often used in confocal microscopy as well. Moreover, both dyes are simultaneously used in multicolor staining [45].

#### 1.2.5.2. Cyanine dyes

Unlike non-water soluble rhodamine, cyanine dyes can be used in aqueous solutions. There are generally two classes of cyanine dyes, mono- and polymethine cyanine dyes (Figure 8). The first group is widely used in nucleic acid labelling. For example, thiazole orange presents poor fluorescence when diluted in a solution. However, when bound to nucleic acid, the fluorescence increases by a factor of 3000 [46].

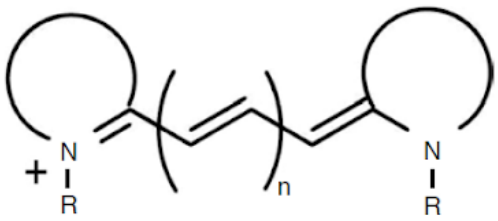


Figure 8: Molecular structure of the family of cyanine dyes. Common names depend on the number of double bonds in polymethine chain (n+1). If n=0, the molecule is referred to as monomethine cyanine. For n=2, the compound is referred to as pentamethine cyanine (or Cy-5). Taken from [47]

This observation is believed to occur because of restriction of the bond between the aromatic rings, preventing non-radiative decay. Similarly to monomethine cyanine dyes, polymethine dyes are also being used for labelling nucleic acids, antibodies and lipids. Since their properties can be easily tuned by introducing the next methine group to the chain, there are dyes designed to emit signal in NIR (near infrared) spectrum [48].

This is favorable when examining biological tissues, because no autofluorescence signal comes from this wavelength region, therefore the signal coming from the sample possess low threshold but also low signal, while the initial elongation of methin chain increases the quantum yield, the further elongation leads to the drop thereof [49].

#### 1.2.5.3. Alexa dyes

Alexa dyes were introduced to overcome some common disadvantages of classic dyes, like their water insolubility (eg. rhodamine, coumarin). Alexa dyes are obtained by introducing sulfonate group, which increases the hydrophilicity of the particle, allowing for bioconjugation in aqueous solutions. Moreover, sulfonation of the dye molecule increases the polarity thereof and prevents aggregation which is preferable, as interaction between molecules decreases their fluorescence yields [50].

This class of dyes cover all wavelength spectrum in terms of excitation and emission, from ultraviolet to red. They are also more photostable and nonsensitive on a broad range of pH. Yet, Alexa dyes possess a net negative charge, which can interfere with positive charged cell cultures [51], therefore neutral dyes may sometimes be a better choice, despite lower fluorescent signal.

### 1.2.5.4. Fluorescent proteins

Another important class of labeling agents is the family of fluorescent proteins. The green fluorescence protein (GFP), was originally extracted from Aequorea victoria jellyfish in 1962. The ability of fluorescence comes from the oxidation and cyclization of Ser-Tyr-Gly sequence in 65-67 position in the protein (Figure 9). It has been proven that GFP does not emit light without the reaction of oxidation [52].

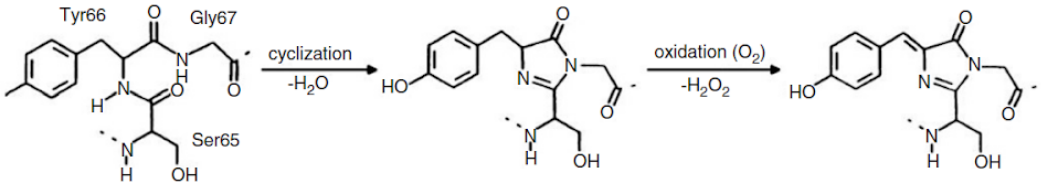


Figure 9: Proposed mechanism of biosynthesis of the chromophore sequence in GFP. Elimination of water upon the nucleophilic attack of the amine group of Gly67 on the carbonyl group of Ser65, results in imidazolidinone ring. Subsequent oxidation by removal of hydrogen atoms from Tyr66 alpha-beta bond introduces a double bond, giving rise to the large delocalized pi-system. Taken from [52]

Removal of hydrogen introduces a double bond which elongates the pi-junction system. Up to date, seven classes of GFP have emerged through mutagenesis studies. Each class exhibits its distinct wavelengths of emission and excitation [24]. GFPs applications as labelling agents are manifold. Since its sequence can be coded into genome and synthesized by the host organism as a tag of any desired protein, it can be used to monitor processes of protein synthesis, protein-protein interactions and chemistry occurring in living cells as it may not interfere with protein function. However, due to high molecular weight (26 kDa), it sometimes influences the folding of the protein of interest, which may affect further interaction with other molecules. Moreover it can cause aggregation of modified proteins and therefore become toxic for the cells. [54].

#### 1.2.5.5. Lanthanide chelates

Lanthanide chelates belong to another group of labeling agents that gain much interest in biological studies. Lanthanides are a group of elements that usually exist as trivalent cations with electronic configuration $4f^n$ with n between 1 ($Ce^{3+}$) to 14 ($Lu^{3+}$). Transitions within 4f shell are responsible for the fluorescent effects. Since this orbital is shielded by orbitals 5s and 5p, it prevents the electrons from external perturbations and therefore the emission spectra are very sharp [55]. Usually, the lanthanide ion is bound to an organic chromophore, which acts as an antenna for absorbing light and transferring the energy to the ion, which itself exhibit inherently weaker absorbance than conventional organic dyes. As and effect, this constructs have a broad range of excitation wavelengths and a sharp, line-like emission peak. The role of the organic ligand is to bind the lanthanide ion, but also as a scaffold for attachment to the reactive group of biomolecules, for example attachment to monoclonal antibody in immunoassays [56]. By varying the lanthanide ions and the antenna, different emission and excitation spectra can be obtained. Because of the long Stokes shift, those labelling agents are useful in the experiments, where problems with sample autofluorescence occur [57]. However, the fluorescent properties of this class of dyes depend on the ability of the ions to bind to the chelating agents. Those are limited to EDTA, DTPA and β-diketonates. As for the ions, Eu(III), Tb(III), Sm(III), and Dy(III) are used [58]

#### 1.2.5.6. Quantum dots

Quantum dots (QD) - semiconductor nanocrystals with the dimensions smaller than the Bohr radius (an average distance between the electron in the conduction band and the hole left in the valence band), from 1-10 nm in diameter. Due to the size, which lays in the same order of magnitude as de Broglie wavelength, those particles exhibit unique optical properties. Those properties were harnessed in imaging, as the particles can emit light with different wavelengths

(upon excitation), depending on the size of the particles (Figure 10). As the size of the particle decreases, the distance between the highest valence band and lowest conduction band increases. Therefore, more energy is emitted when the dot comes back to the ground state which results in the emission of the blue-shifted wavelength. Moreover, QDs exhibit continuous absorption, thus can be excited with any wavelength shorter than emitted, which makes them promising candidates for multicolor imaging [58]

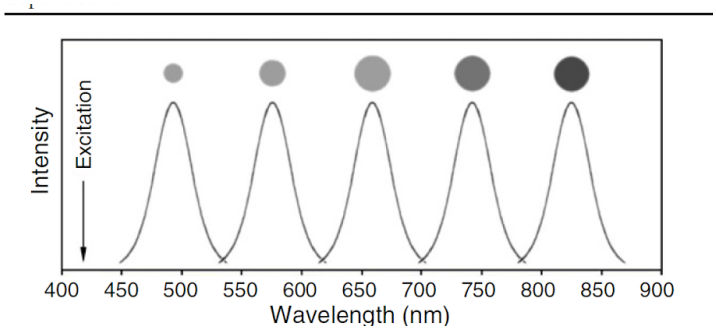


Figure 10: The emission spectrum of the QDs can be tuned by altering the size of the molecules. Taken from [43]

QDs show superior behavior over traditional dyes, mostly due to their high luminescence and high resistance to photobleaching. However, QDs are initially non-biocompatibile, thus their hydrophobic surface has to be altered the attachment of amphiphilic moieties, like phospholipids or amphiphilic polysaccharides [59].

## 1.3. Stimuli-responsive Nanomedicines

Pharmaceutical therapeutics often suffer from short half-lives, rapid clearance and poor bioavailability. Therefore higher doses and more often applications are required which can result in cytotoxicity, when the drug binds non-specifically with a different receptor. In contrast, nanomedicines offer a platform to deliver the active therapeutic ingredient (API) specifically to the site of action and facilitate controlled release thereof. As a result, lower dosage can be administered with simultaneous increase of the efficiency. Those vehicles can release their cargo upon local deviations in microenvironment, such as changes in pH and redox potential or enzymes overexpression. They can also be responsive to the external physical stimuli, ultrasound, light or temperature [60].

Materials utilised in nanomedicine include co-polymers, dendrimers, hyperbranched polymers, micelles and liposomes. The active agent can be either encapsulated or chemically bound to the carrier with the environment-sensitive linker. Nanoscale of those vehicles and their architecture allow them to cross the biological barriers and interact with the receptors on the cell surface [61].

The release of the API in the site of action can occur due to the degradation of the carrier or difference in the charge of the functional groups. This approach applies to the situation where the active agent in entrapped inside the carrier. In case of chemically linked conjugate of the carrier and the API, the release of the cargo is done by the cleavage of the linker between the agent and the carrier. Both modes of action are depicted in Figure 11.

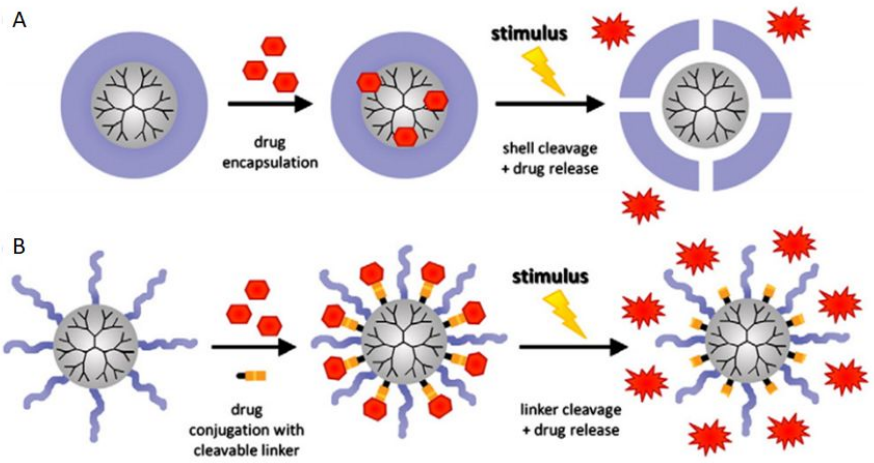


Figure 11: Different strategies for the release of the active agent upon an external stimuli. The API can either be released by the degradation of the encapsulating vehicle (A), or by the cleavage of the linker between the API and the carrier (B). Taken from: [60]

The chemical stimuli for the triggered drug release include change in pH, enzyme overexpression in the sites of pathological changes or antigen-antibody interactions [62]. It is known that in tumorous tissue pH is altered towards more acidic compared to physiological pH (6-7 compared to 7.4, respectively) [63]. For example, a N-(2-hydroxylopropyl)-methacrylamide (HPMA) polymer with hydrazone linker, was used to conjugate and deliver an anticancer drug, doxorubicin into the tumorous tissue. The conjugate remained stable in the systemic pH, however upon the pH-gradient in the tumor, the drug was successfully released [64]. Therefore conjugation of the API with a pH-sensitive linker could facilitate a smart release upon the recognition of that pH-gradient.

Tumorous tissue often exhibits an overexpression of estreases and proteases. Such behaviours was used in designing enzyme-responsive nanocarriers, which use short peptides as a substrate for those enzymes. HPMA polymer conjugated with doxorubicin by the Gly–Phe–Leu–Gly linker allowed for a controlled release in the tumor site. The linker is a substrate for cathepsin B, which is a lysosomal enzyme often overexpressed in tumor cells. Hydrolysis thereof facilitated the liberation of the active agent [65].

In the malignant tissues, poor vasculature results in hypoxic environment, which is rich in one- or two- electron reducing enzymes, such as cytochrome c reductase. This reductive system can be harnessed to liberate the active ingredient, due to the breakdown of disulfide bonds which can be incorporated in the vehicle scaffold by thiol-containing moieties [66].

Some polymers exhibit a lower critical solution temperature (LCST), above which, the balance between hydrophilicity and hydrophobicity is disturbed. Heated to the temperature higher than LCST results in dehydration of the polymer backbone and increase in lipophilicity. In this situation such a polymer will collapse. Micelles containing a thermo-sensitive polymer will disassemble and release the payload in the site of action. The increase in temperature appears in some tumors or can be induced by external radiation applied locally. Poly(N-isopropylacrylamide) (PNIPAAM) seems to be a promising candidate for this purpose, as its LCST is 32*C, above a rapid phase transition occurs. Since PNIPAAM is non-toxic and the LSCT is close to human's body temperature, this polymer has been examined for medical applications. Furthermore, the co-polymerization with more hydrophilic polymers, like dendritic polyglycerol, increased the LCST and prevented the conjugate from precipitation when heated above 32*C [67]. Biological systems were also found to have thermal-responsiveness. For example collagen contains glycine–proline–(hydroxy)proline (Gly–Pro–Pro(Hyp)) sequence, which is repeated to from a triple-helix structure, which dissociates at melting temperature. Co-polymerization of collagen-like peptide with dendritic polymers yields a temperature-sensitive drug delivery system [68].

Along side of the controlled release of an active entity, nanocarriers exhibit also a targeting abilities, which allow them to reach specifically the pathological site of the body and liberate the cargo directly. There are two major approaches utilized for selective delivery. Active targeting includes attaching an antibody on the surface of the vehicle. Tumor cells express specific antigens and receptors. Once identified, they can be recognized with dedicated antibodies that will bind to them exclusively and release the cargo in the malignant tissue, while sparing the healthy one. Passive targeting on the other hand, utilises the phenomenon called enhanced permeation and retention effect (EPR), which refers to fenestrated epithelium of the poorly formed new blood vessels around the tumor, however this effect was also observed in the inflammation sites. Due to bigger pores in the endothelium, a high MW molecules can enter and remain for a long period of time, increases the chance of releasing the active agent upon external stimuli (enzymatic cleavage, or low pH) [69].

Among polymeric nanocarriers, dendritic polymers are widely studied, due to their monodispersity and high amount of surface groups, which allows to bind the active agent, a ligand for active targeting and/or imaging probe. However, the major drawback is the tedious synthesis which requires several synthetic steps and after each of them the generation of the polymer is only extended by one. In contrast, hyperbranched polymers exhibit similar properties

to dendrimers, like high number of reactive surface groups, however they can be synthesised in a one-pot reaction, for example ring-opening multibranching polymerization. Low polydispersity can be achieved by slow monomer addition. Among hyperbranched polymers, hyperbranched polyglycerol (hPG) keep gaining more and more attention, due to the high biocompatibility, high stability and hydrophilicity and achievable low polydispersity [70]. hPG contains a large number of hydroxyl groups on the surface, which can be further converted to e.g. amine groups or conjugated with cleavable ester bond for binding an API. An example of such a drug delivery system is depicted in Figure 12.

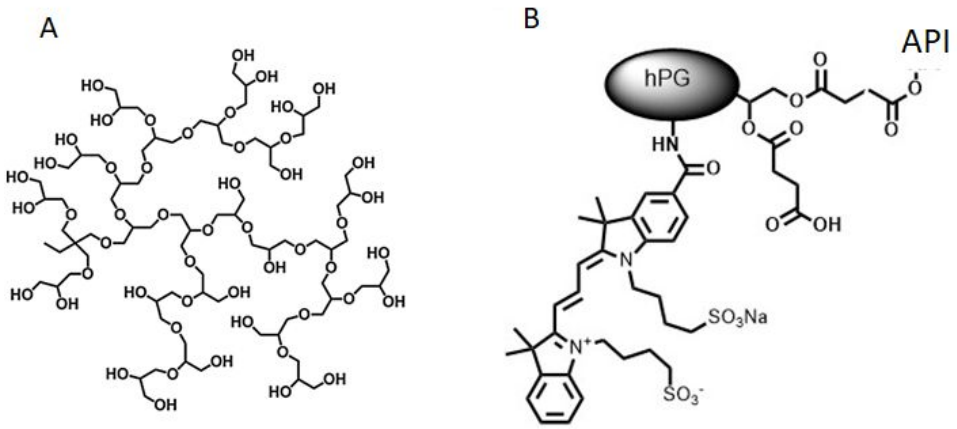


Figure 12: (A) hPG molecule, adapted from: [70]. (B) an example of Cy3-labelled hPG polymer conjugated with the API via a cleavable ester bond. Conversion of the -OH into -$NH_2$ allows for dye conjugation by a stable amide bond.

# 2. Objectives

Since nanomaterials are being more and more widely used in medicine as therapeutic agents, delivery vehicles and imaging agents, there is an increased need to deliver the data which reflect the behaviour of nanocarriers in the organism. The following project aimed to assess the biodistribution and preferable pathways of elimination of four fluorescently labeled hPG-based conjugates and recognize the differences between their behaviour *in vivo* due to their molecular mass and surface charge. The difference in the distribution was also discussed in respect to two injection types, intravenous and subcutaneous.

Presence of the conjugates within the examined organs is to be assessed quantitatively and qualitatively by means of fluorescence microscopy. The quantitative analysis was performed by measuring the intensity of fluorescence in a computer software with respect to the previously prepared calibration curve, obtained from the images of the diluted Cyanine 3 (Cy3) dye.

Additionally, the spectrofluorimetric analysis of urine was performed for rats treated i.v. hPG-Cy3 and hPG-Cy3-Succ, in order to assess the excretion rate after 2h and 6h from injection. The concentrations were also calculated with respect to prepared calibration curves.

# 3.Materials and methods

## 3.1. Sample substances

Four conjugates were used for the biodistribution studies of Cy3-labelled hPG-based drug delivery system. Additionally, mere Cy-3 is also going to be used as a control. Conjugates used for the research:

1. 10 kDa hPG with 2% -OH groups converted to -$NH_2$ . The Cy-3 dye is covalently bound to amine groups with a degree of functionalization (DF): 0.43%.
   Molecular mass: 11 kDa

2. 10 kDa hPG with 2% -OH groups converted to -$NH_2$ for Cy-3 binding and succinic anhydride (Succ) conjugated to hydroxyl groups via ester bond.
   Cy-3 DF: 0.66%
   Succ DF: 81.75%
   Molecular mass: 23 kDa

3. 10 kDa hPG with 2% -OH groups converted to -$NH_2$ for Cy-3 binding and succinic anhydride conjugated to hydroxyl groups via ester bond. API coupled with succinic linker via ester bond as well.
   Cy-3 DF: 0.34%
   Succ DF: 84.59%
   API DF: 6.9%
   Molecular mass: 25 kDa

4. 10 kDa hPG with 2% -OH groups converted to -$NH_2$ for Cy-3 binding and succinic anhydride conjugated to hydroxyl groups via ester bond. API coupled with succinic linker via ester bond as well.

Cy-3 DF: 0.42%

Succ DF: 92.73%

API DF: 3.46%

Molecular mass: 24 kDa

The dilutions calculated for the injections refer to the Cy-3 content of each construct, which should be an equivalent to 0.231 mg (0.000347 mmol) of Cy-3 / kg of rat body weight. Accordingly, the amounts of each constructs per kg of rat body weight are as follows:

6.211 mg/kg for hPG-Cy3

7.684 mg/kg for hPG-Cy3-Succ

18.185 mg/kg for hPG-Cy3-Succ-API (7%)

14.762 mg/kg for hPG-Cy3-Succ-API (3.5 %)

0.231 mg/kg for pure Cy-3

API - morphine-derivative opiate molecule with the MW~350 g/mol and tertiary amine group protonated in pH<9

## 3.2. Experimental animals, housing and grouping

Group of 24 male rats Wistar was provided by Charité - Universitätsmedizin Berlin. Body mass of each rat was in range 250-400 g. All rats had induced inflammation of a left paw. Animals were housed at room temperature under standard “enriched” cage environments and had free access to regular rodent chow and drinking water. A 12h/12h light-dark-cycle was applied.

Animals were grouped to allow already familiar animals to stay with each other to reduce stress of the animals. Animals were assigned to groups and acclimatised to their respective cages at least 7 days before the experimental start.

## 3.3. Treatment and doses

All the constructs were administered into rats either as an intravenous (i.v.) injection in tail vein or subcutaneous (s.c.) injection in the neck. The dilutions were made in 0.9% w/v saline. The concentrations were adjusted in the manner, that the maximum volume to be injected was 300 µL. The same concentrations of the tested substance were used regardless the type of the injection. The dosage dependence on rat body weight is presented below (Table 1).

| Rat weight (kg) | Injection volume (mL) | Mass of injected substance (mg) | | | | |
|---|---|---|---|---|---|---|
| | | hPG-Cy3-Succ-API 7% | hPG-Cy3-Succ-API 3.5% | hPG-Cy3-Succ | hPG-Cy3 | Cy3 |
| 0.180 | 0.135 | 2.66 | 3.27 | 1.38 | 1.12 | 0.04 |
| 0.190 | 0.143 | 2.80 | 3.46 | 1.46 | 1.18 | 0.04 |
| 0.200 | 0.150 | 2.95 | 3.64 | 1.54 | 1.24 | 0.05 |
| 0.210 | 0.158 | 3.10 | 3.82 | 1.61 | 1.30 | 0.05 |
| 0.220 | 0.165 | 3.25 | 4.00 | 1.69 | 1.37 | 0.05 |
| 0.230 | 0.173 | 3.40 | 4.18 | 1.77 | 1.43 | 0.05 |
| 0.240 | 0.180 | 3.54 | 4.36 | 1.84 | 1.49 | 0.06 |
| 0.250 | 0.188 | 3.69 | 4.55 | 1.92 | 1.55 | 0.06 |
| 0.260 | 0.195 | 3.84 | 4.73 | 2.00 | 1.61 | 0.06 |
| 0.270 | 0.203 | 3.99 | 4.91 | 2.07 | 1.68 | 0.06 |
| 0.280 | 0.210 | 4.13 | 5.09 | 2.15 | 1.74 | 0.06 |
| 0.290 | 0.218 | 4.28 | 5.27 | 2.23 | 1.80 | 0.07 |
| 0.300 | 0.225 | 4.43 | 5.46 | 2.31 | 1.86 | 0.07 |
| 0.310 | 0.233 | 4.58 | 5.64 | 2.38 | 1.93 | 0.07 |
| 0.320 | 0.240 | 4.72 | 5.82 | 2.46 | 1.99 | 0.07 |
| 0.330 | 0.248 | 4.87 | 6.00 | 2.54 | 2.05 | 0.08 |
| 0.340 | 0.255 | 5.02 | 6.18 | 2.61 | 2.11 | 0.08 |
| 0.350 | 0.263 | 5.17 | 6.36 | 2.69 | 2.17 | 0.08 |
| 0.360 | 0.270 | 5.31 | 6.55 | 2.77 | 2.24 | 0.08 |
| 0.370 | 0.278 | 5.46 | 6.73 | 2.84 | 2.30 | 0.09 |
| 0.380 | 0.285 | 5.61 | 6.91 | 2.92 | 2.36 | 0.09 |
| 0.390 | 0.293 | 5.76 | 7.09 | 3.00 | 2.42 | 0.09 |
| 0.400 | 0.300 | 5.91 | 7.27 | 3.07 | 2.48 | 0.09 |

Table 1: Weight dependent injection volumes and corresponding mass of injected substance

## 3.4. Sacrifice of rats and samples collection

60 min after injection, the animals were sacrificed for examination of the organs and blood smears and blood samples for serum isolation.

Initial deep anaesthesia (Isoflurane: 5 vol. %, $O_2$: 2 L/min) was followed by ketamine injection in the abdominal cavity and maintenance anaesthesia (isoflurane: 3-4 vol. %, $O_2$: 1 L/min) until exsanguination. Following steps were performed to collect the samples:

- Opening of peritoneum and blood drain from aorta via cannulation for blood smear and serum (serum was prepared by centrifuging the blood samples for 5 min /3000 rpm and subsequent transfer to other tube and stored in -20°C)
- Perfusion with 40-50 ml PBS / 5% (v/v) glycerin after opening central vein. The perfusion was carried out until the organs were no longer getting cleared from the blood.
- Cutting out the heart to ensure the death of animal.
- Collecting the following organs:
  - Brain (left hemisphere of the brain)
  - Spleen (middle piece)
  - Kidney (right - whole organ)
  - Liver (top hepatic lobe)
  - Lung (lower lobe)
  - Inflamed paw
  - Non-inflamed paw
- After collection of each organ, it was washed in PBS / 5% (v/v) glycerin and embedded in a cryomold using TissueTek O.C.T. compound (Sakura). Organs prepared in that manner were left to freeze on dry ice (-80°C) and further stored in (-80°C).

## 3.5. Cryosectioning

Collected organs were mounted on the sectioning platform within the cryostat (Thermo Scientific) using TissueTek. Temperature of the sample was set to -18°C and the temperature of the cutting blade was set to -25°C. Obtained sections of 20 µm thickness were placed on microscope slides (Superfrost Plus, R. Langenbrinck Labor- u. Medizintechnik) and mounted using DAPI mounting medium.

## 3.6. Fluorescent microscopy analysis

The signal from dye-labelled constructs or mere dye was detected and documented in the Biorevo Keyence BZ-9000 fluorescence microscope with an incorporated digital camera, using BZII Viewer software. For Cy3 signal, TRITC filter was used (excitation 543/22 nm, emission 593/40 nm fluorescence filter; Keyence), x40 PlanApo NA 0.95 Objective and exposure times ½ s, ¼ s, ⅛ s. For kidney additional exposure time of 1/12 s was used exclusively. Each fluorescent picture was also documented using brightfield settings: 1/1400s exposure time, 60% lighting (quantity), 50% lighting (stop), 100% light quantity. Additionally, the same viewfield was also documented using DAPI-B filter (excitation 360/40 nm, emission 460/50 nm). All obtained images were saved as 1360 x 1024 pixel .TIFF files.

Moreover, images of dye dilutions with known concentrations were obtained. The volume of each dilution on the slide was adjusted in a way that the thickness of the examined sampled was equal to the thickness of the organ sections analyzed (20 µm).

## 3.7. Fluorescence intensity quantification

"ImageJ" software was used to assess the Cy3 fluorescence intensity of the images obtained by fluorescence microscopy analysis. The integrated density was calculated in the software for each image. Also, a mean integrated density value was measured for each organ type from rats from the control group (with no substance injected). Subsequently, the appropriate value was subtracted from the integrated density of each organ image of the remaining groups.

Additionally, images of dye dilutions of known concentration obtained by means of fluorescence microscope were assessed using the same software (ImageJ). After subtraction of the blank from each image of corresponding concentration, two calibration curves were obtained for calculating the constructs concentrations in different organs.

## 3.8. Spectrofluorometric analysis

Spectrofluorimetry of urine was made for the rats taken from the second phase of the research, using the Jasco-6500 spectrofluorometer. Two groups of four rats treated hPG-Cy3 (8.26 mg/kg body weight) i.v. and two groups of four rats treated hPG-Cy3-Succ (18.27 mg/kg body weight) i.v. were sacrificed, after 2h and 6h. Prior to sacrifice, they were kept in metabolic cages and their urine was collected. The spectrofluorimetry was made to assess the percentage of the conjugate excreted after the corresponding time. The concentration was calculated from the two calibration curves obtained by measuring the emission signal of the series of solutions with known concentration. Average mass of the animal was 350 mg and the average dose of the conjugate was 2.9 mg/mL and 6.4 mg/mL for hPG-Cy3 and hPG-Cy3-Succ, respectively.

# 4. Results

## 4.1. Morphological analysis during dissection

The type of injection was confirmed by visual assessment of the opened (through cutting the skin) injection site. Pink stained area around the injection site proved the right subcutaneous injection. If injected intravenously, no stains around the injection site were observed. Instead the mere vein was coloured slightly pink. The aim was to have an equal number of i.v. and s.c. injection. However, in some i.v. attempts into the tail vein, a bulb in a vein appeared. Subsequent cut through the tail showed the pinkish adjacent site. Those cases were later considered as a s.c. injection. The weights of the rats and the type of injection of each construct was presented below in Table 2.

| Rat number | Rat weight (g) | Substance and dosage (mg/kg body weight) | Type of injection |
|---|---|---|---|
| 2.1 | 402 | hPG-Cy3-Succ-API (7%) 14.76 mg/kg | s.c. 1x |
| 2.2 | 377 | | s.c. 1x |
| 6.1 | 302 | | i.v. 1x |
| 6.2 | 291 | | i.v. 1x |
| 3.1 | 339 | hPG-Cy3-Succ-API (3.5%) 14.76 mg/kg | i.v. 1x |
| 3.2 | 302 | | i.v. 1x |
| 4.1 | 285 | | s.c. 1x |
| 4.2 | 321 | | s.c. 1x |
| 5.1 | 354 | hPG-Cy3-Succ 7.68 mg/kg | i.v. 1x |
| 5.2 | 349 | | s.c. 1x |
| 5.3 | 367 | | i.v. 1x |
| 5.4 | 351 | | i.v. 1x |
| 7.1 | 403 | hPG-Cy3 6.21 mg/kg | i.v. 1x |
| 7.2 | 349 | | s.c. 1x |
| 7.3 | 382 | | s.c. 1x |
| 7.4 | 353 | | s.c. 1x |
| 8.1 | 393 | 0.23 mg/kg | i.v. 1x |
| 8.2 | 379 | | i.v. 1x |
| 8.3 | 397 | | s.c. 1x |
| 8.4 | 330 | | s.c. 1x |

Table 2: Rat weights and type of injection of a conjugate with a given dosage

## 4.2. Image acquisition and qualitative visual assessment of the fluorescence signal

### 4.2.1. Brain

The visual assessment of the obtained images showed no signal of Cy3 dye, nor any labelled conjugate, regardless the type of injections. The DAPI staining clearly visualized the cells' nuclei. Examples of the obtained signals after i.v. and s.c. injections are presented in Figure 13 and 14, respectively

### 4.2.2. Liver

Visual assessment of the liver showed fluorescence signal from rats treated with hPG-Cy3-Succ-API 7% and 3.5%, as well as hPG-Cy3-Succ, regardless the type of injection. No signal was observed in rats treated with hPG-Cy3, nor mere Cy3 dye. Examples of the obtained signals after i.v. and s.c. injections are presented in Figure 15 and 16, respectively. The DAPI staining visualized the cells' nuclei, however in some cases the signal appeared blurry, where single signals from the nuclei could not be distinguished (Image 16H).

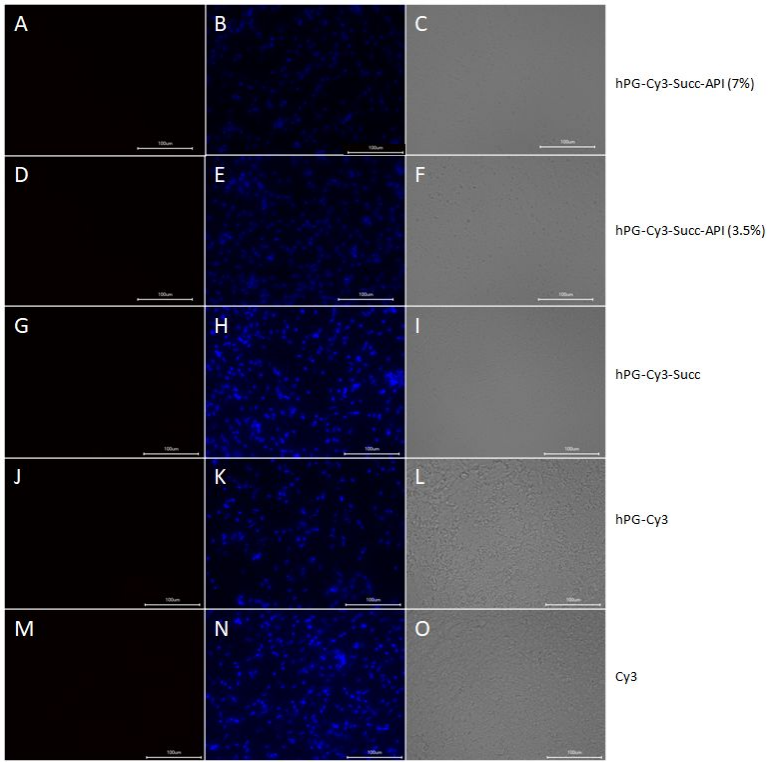


Figure 13: Brain images obtained by means of fluorescent microscopy (i.v. injection). Left column - images with TRITC filter (exp. Time 1/2s). Middle column - images with DAPI-B filter. Right column - brightfield (exp. Time 1/1400s). Scale bar: 100 µm

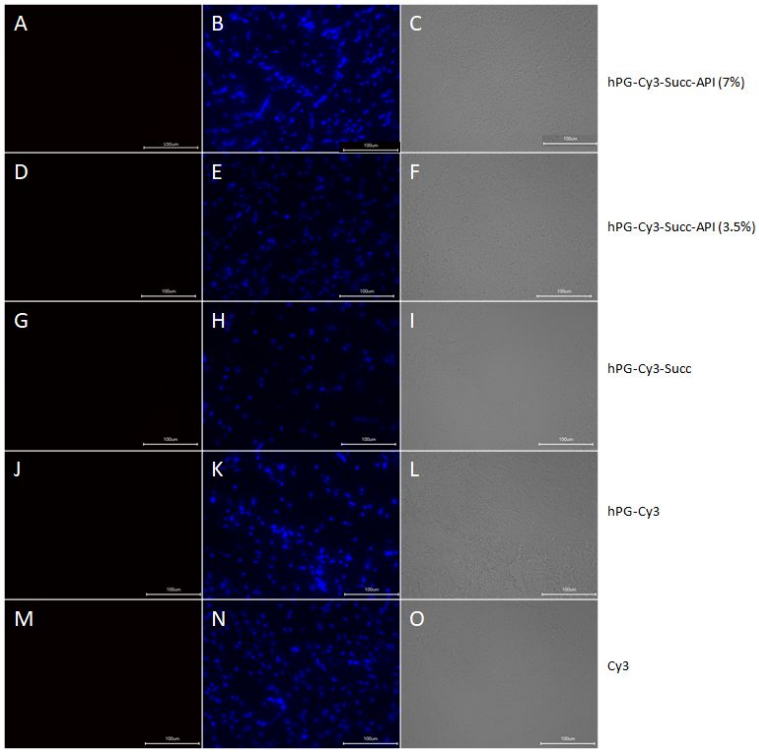


Figure 14: Brain images obtained by means of fluorescent microscopy (s.c. injection). Left column - images with TRITC filter (exp. Time 1/2s). Middle column - images with DAPI-B filter. Right column - brightfield (exp. Time 1/1400s). Scale bar: 100 µm

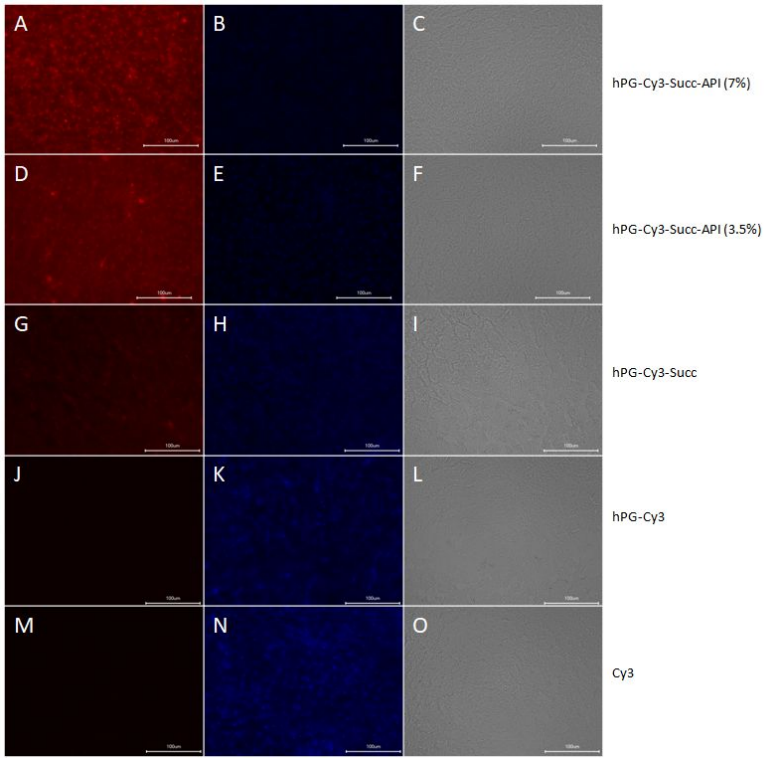


Figure 15: Liver images obtained by means of fluorescent microscopy (i.v. injection). Left column - images with TRITC filter (exp. Time 1/2s). Middle column - images with DAPI-B filter. Right column - brightfield (exp. Time 1/1400s). Scale bar: 100 µm

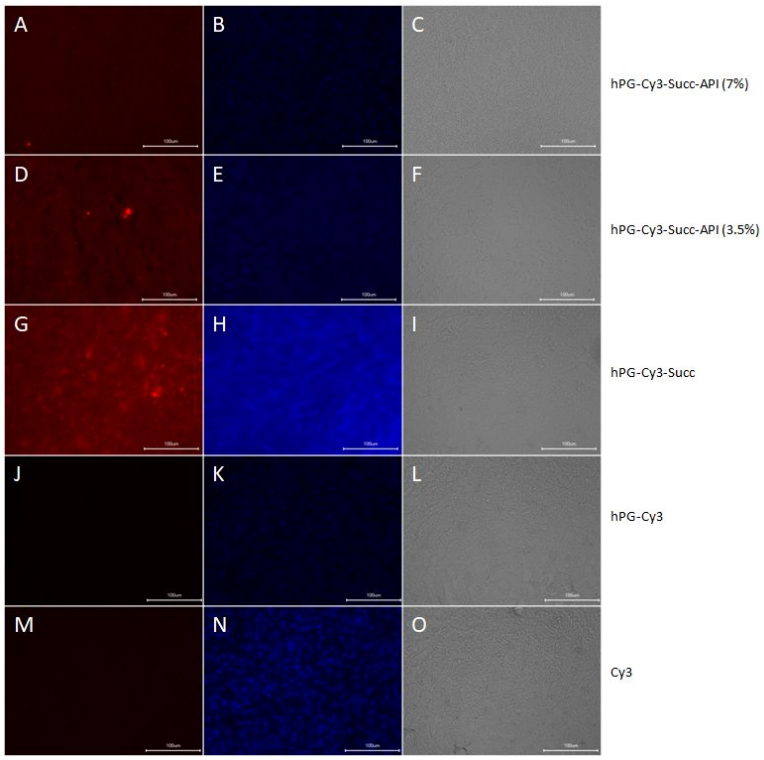


Figure 16: Liver images obtained by means of fluorescent microscopy (s.c. injection). Left column - images with TRITC filter (exp. Time 1/2s). Middle column - images with DAPI-B filter. Right column - brightfield (exp. Time 1/1400s). Scale bar: 100 µm

### 4.2.3. Lung

The strongest fluorescence signal from the lung was observed as single dots in rats treated hPG-Cy3-Succ-API 7% injected i.v.. The fluorescence signal was also noticed in rats treated hPG-Cy3-Succ-API 3.5% (i.v. and s.c.) and hPG-Cy3-Succ (s.c.). For latter conjugates the signal appeared much weaker, but considered as with similar intensity. No visual signal was observed in rats treated hPG-Cy3 or mere Cy3, regardless the type of injection. Examples of the obtained signals after i.v. and s.c. injections are presented in Figure 17 and 18, respectively.

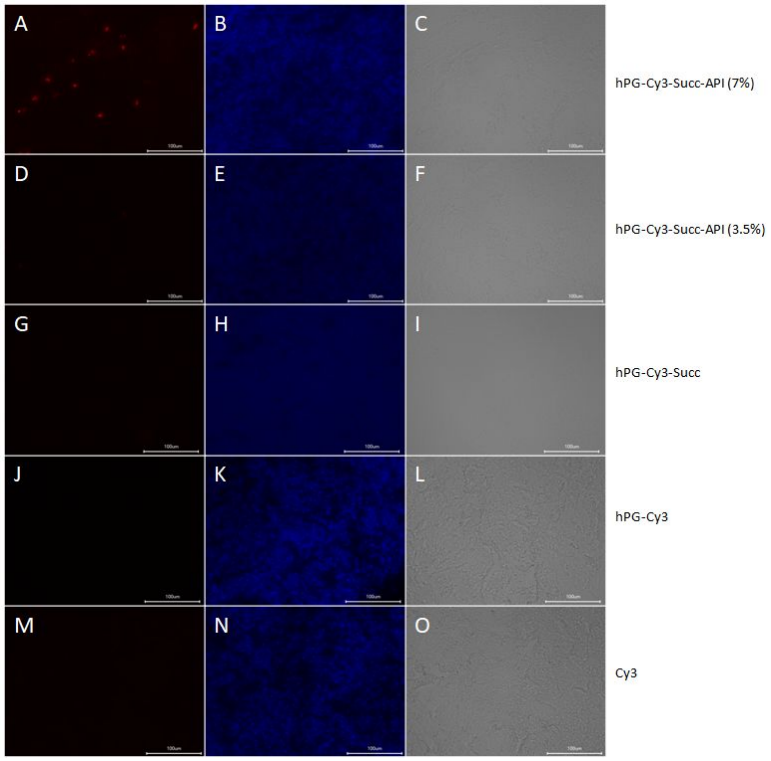


Figure 17: Lung images obtained by means of fluorescent microscopy (i.v. injection). Left column - images with TRITC filter (exp. Time 1/2s). Middle column - images with DAPI-B filter. Right column - brightfield (exp. Time 1/1400s). Scale bar: 100 μm

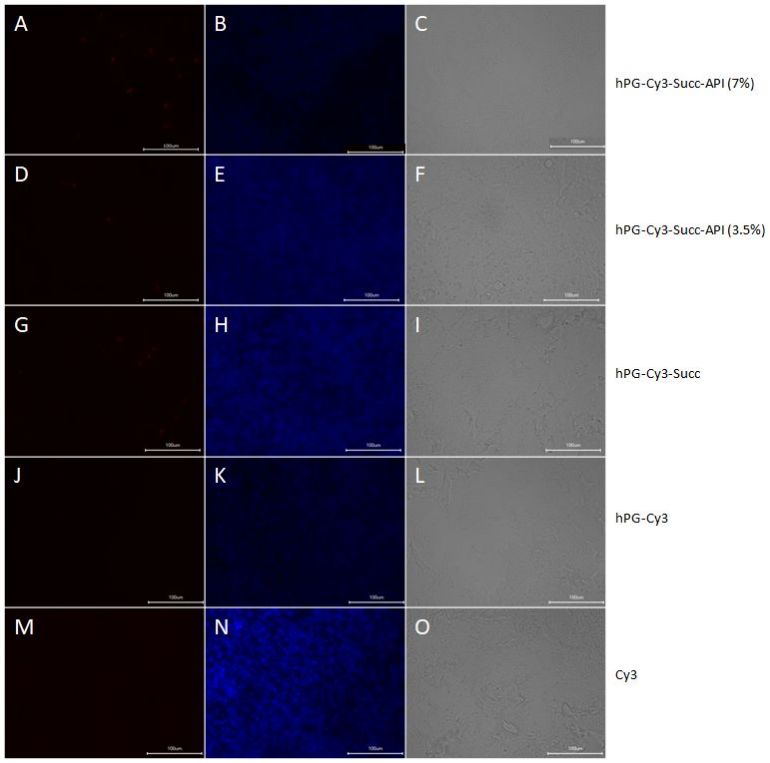


Figure 18: Lung images obtained by means of fluorescent microscopy (s.c. injection). Left column - images with TRITC filter (exp. Time 1/2s). Middle column - images with DAPI-B filter. Right column - brightfield (exp. Time 1/1400s). Scale bar: 100 μm

### 4.2.4. Spleen

The fluorescent signal was observed in rats treated with hPG-Cy3-Succ-API 7% and 3.5%, as well as hPG-Cy3-Succ, regardless the type of injection. However, in rats treated i.v., the signal is more evenly distributed throughout the organ, whereas in s.c. cases, it appears more as aggregated red dots. No signal was observed in rats treated with hPG-Cy3, nor mere Cy3. Examples of the collected images after i.v. and s.c. injections are presented in Figure 19 and 20, respectively.

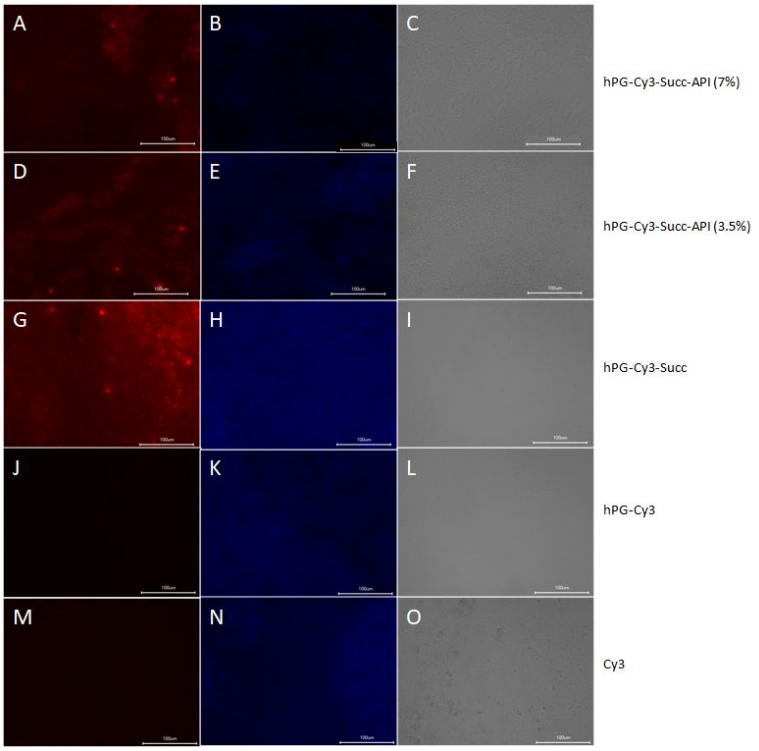


Figure 19: Spleen images obtained by means of fluorescent microscopy (i.v. injection). Left column - images with TRITC filter (exp. Time 1/2s). Middle column - images with DAPI-B filter. Right column - brightfield (exp. Time 1/1400s). Scale bar: 100 µm

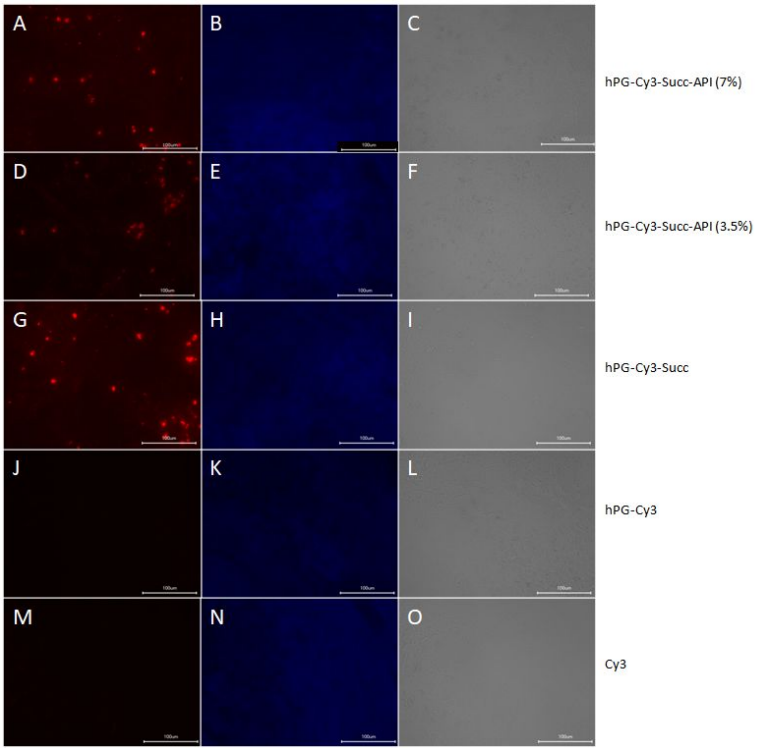


Figure 20: Spleen images obtained by means of fluorescent microscopy (s.c. injection). Left column - images with TRITC filter (exp. Time 1/2s). Middle column - images with DAPI-B filter. Right column - brightfield (exp. Time 1/1400s). Scale bar: 100 µm

### 4.2.5. Kidney

Due to the over saturation of the images of the kidney at exp. time of 1/2s, another exp. time of 1/18s has been chosen for this organ. The signal appears in rats treated with hPG-Cy3-Succ-API 7% and 3.5%, as well as hPG-Cy3-Succ. In rats treated with hPG-Cy3, the signal was only seen in shorter exposure time (1/2s), and appear to be weaker than in the case of the bigger constructs. By visual assessment, it can be observed that in i.v. cases the signal is stronger than in rats treated by s.c. injection. For i.v., the strongest signal comes from hPG-Cy3-Succ-API 7%, whereas for s.c. injections the strongest signal was observed in hPG-Cy3-Succ. Examples of the collected images after i.v. and s.c. injections are presented in Figure 21 and 22, respectively.

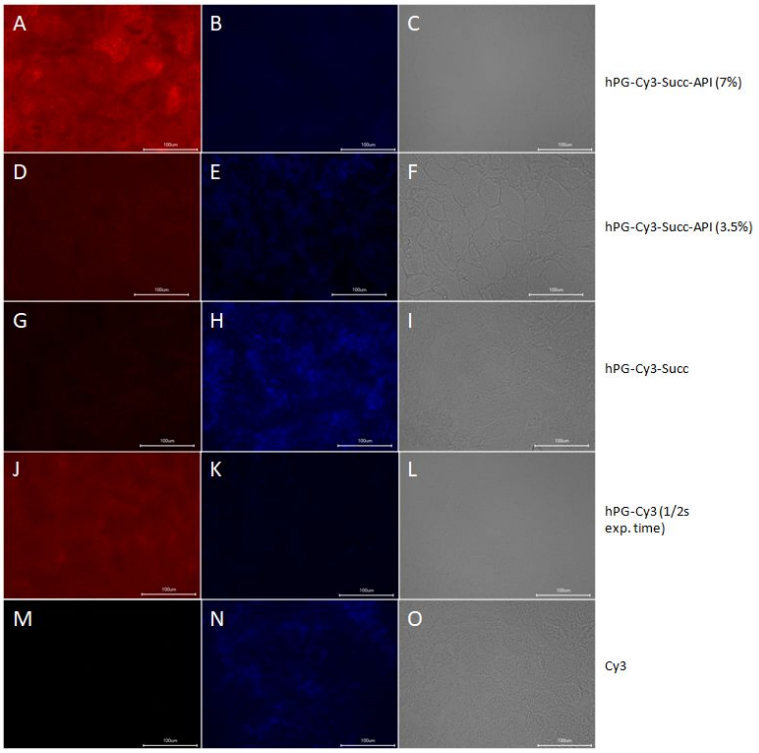


Figure 21: Kidney images obtained by means of fluorescent microscopy (i.v. injection). Left column - images with TRITC filter (exp. Time 1/12s and 1/2s for hPG-Cy3). Middle column - images with DAPI-B filter. Right column - brightfield (exp. Time 1/1400s). Scale bar: 100 µm

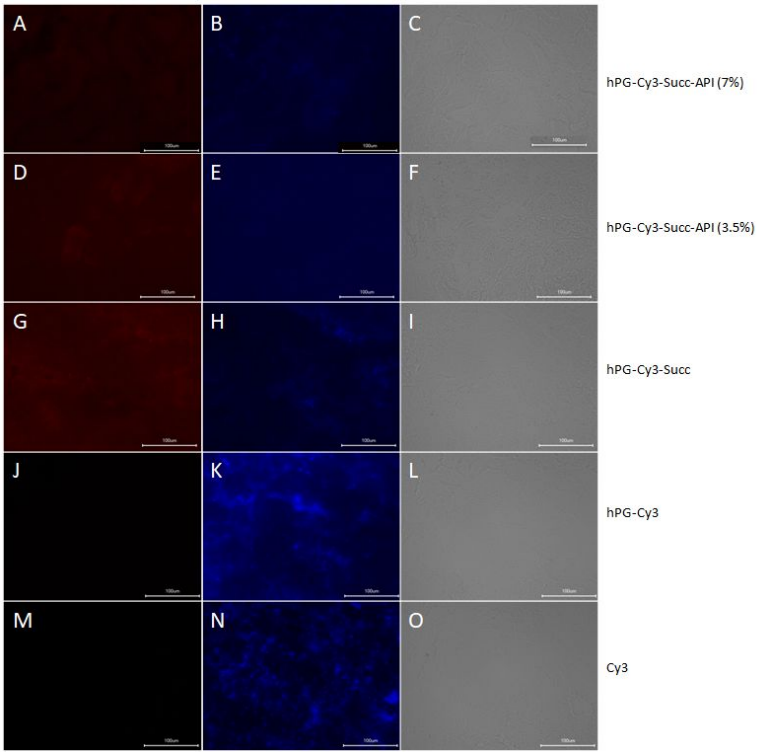


Figure 22: Kidney images obtained by means of fluorescent microscopy (s.c. injection). Left column - images with TRITC filter (exp. Time 1/12s). Middle column - images with DAPI-B filter. Right column - brightfield (exp. Time 1/1400s). Scale bar: 100 μm

### 4.2.6. Control Paw

No fluorescence signal could be visually detected in the control paw in any rat groups, regardless of the type of injection. Examples of the collected images after i.v. and s.c. injections are presented in Figure 23 and 24, respectively.

### 4.2.7. Inflamed Paw

Signal from the inflamed paw was only observed in case of i.v. injected rats treated with hPG-Cy3-Succ-API 7% and 3.5%, as well as hPG-Cy3-Succ. There was an observed pattern, in which the signal was aggregating within one specified area, appearing as an agglomeration of red dots. No visual signal was noticed from s.c. treated rats, nor hPG-Cy3 and Cy3 treated rats, regardless of the type of injections. Examples of the collected images after i.v. and s.c. injections are presented in Figure 25 and 26, respectively.

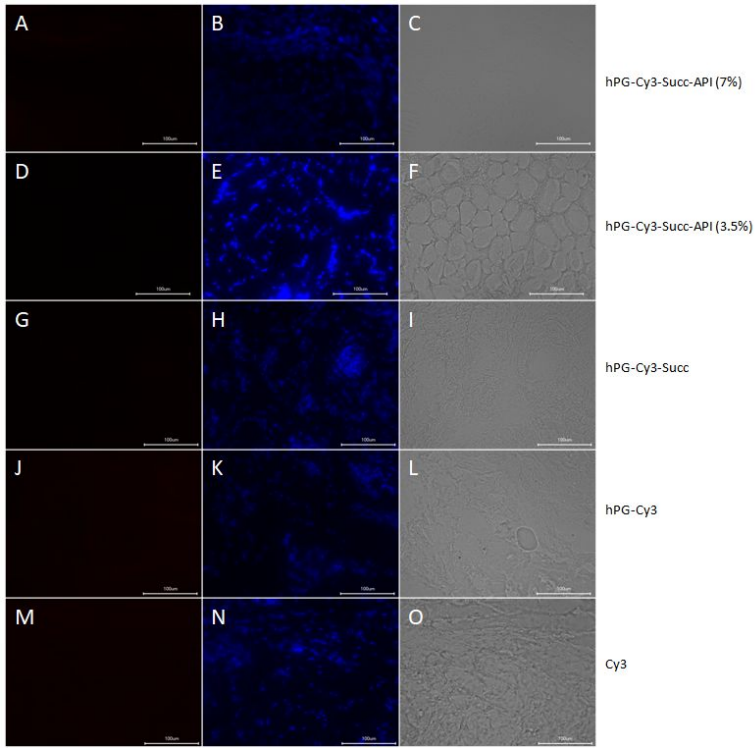


Figure 23: Control paw images obtained by means of fluorescent microscopy (i.v. injection). Left column - images with TRITC filter (exp. Time 1/2s). Middle column - images with DAPI-B filter. Right column - brightfield (exp. Time 1/1400s). Scale bar: 100 µm

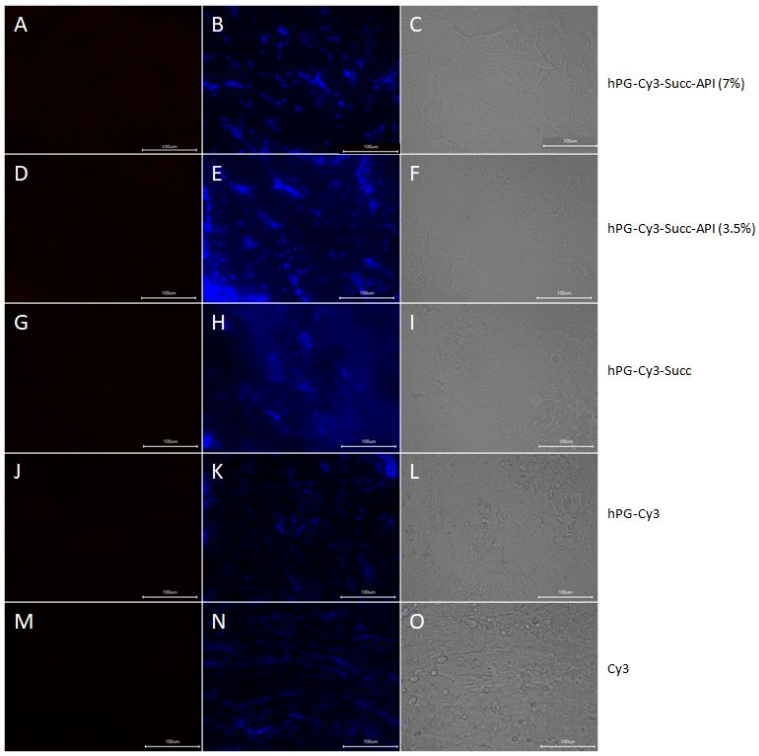


Figure 24: Control paw images obtained by means of fluorescent microscopy (s.c. injection). Left column - images with TRITC filter (exp. Time 1/2s). Middle column - images with DAPI-B filter. Right column - brightfield (exp. Time 1/1400s). Scale bar: 100 µm

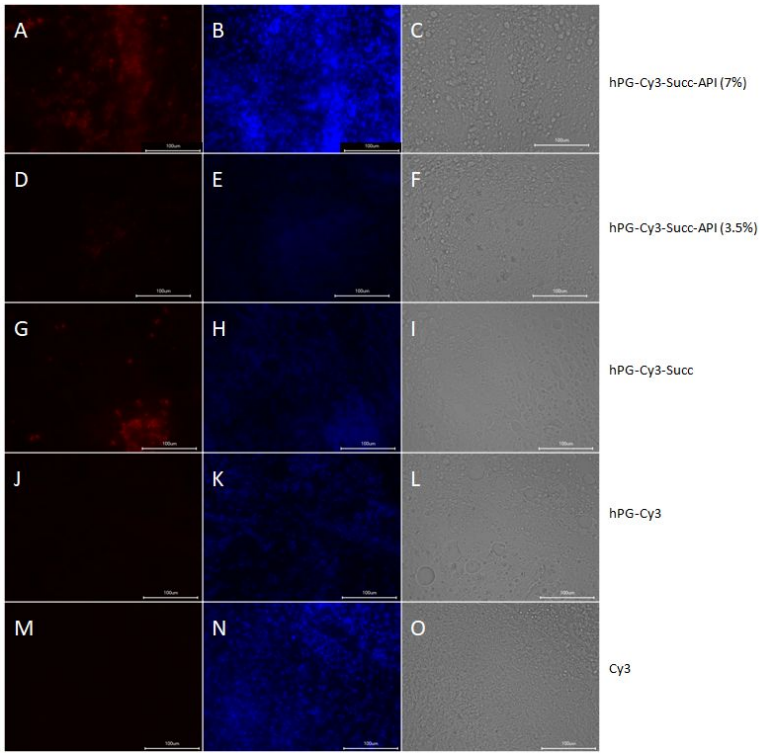


Figure 25: Inflamed paw images obtained by means of fluorescent microscopy (i.v. injection). Left column - images with TRITC filter (exp. Time 1/2s). Middle column - images with DAPI-B filter. Right column - brightfield (exp. Time 1/1400s). Scale bar: 100 µm

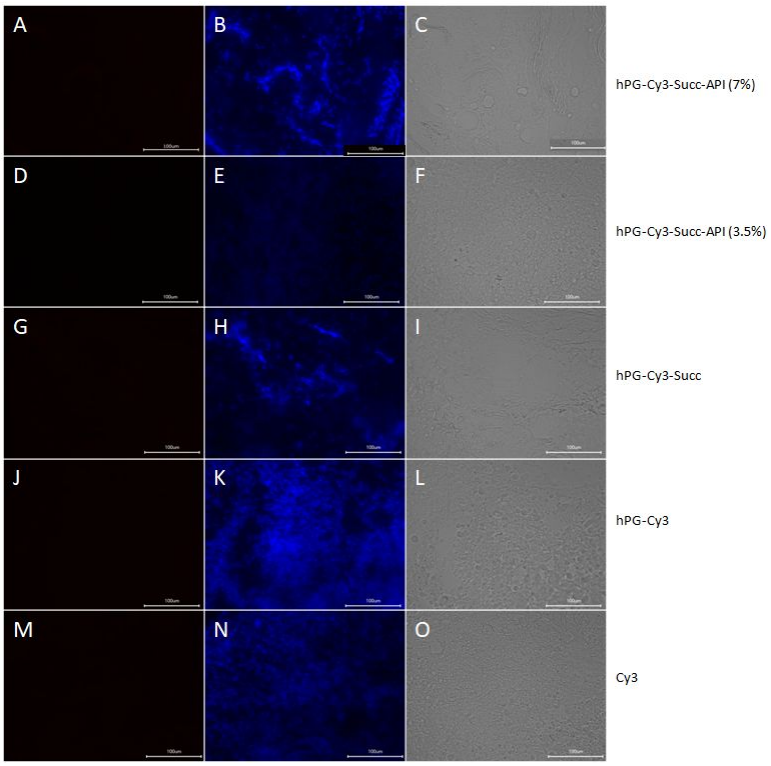


Figure 26: Inflamed paw images obtained by means of fluorescent microscopy (s.c. injection). Left column - images with TRITC filter (exp. Time 1/2s). Middle column - images with DAPI-B filter. Right column - brightfield (exp. Time 1/1400s). Scale bar: 100 µm

## 4.3. Relative quantification of autofluorescence signal in different organs.

The fluorescence intensity quantification was determined automatically by means of the computer software (ImageJ). The Integrated Density values obtained from the images were averaged within the group. The standard deviation was calculated for all of images for organ from one group. Subsequently the background fluorescence signal from control group (no treatment) was subtracted. All images were obtained in 40x magnification and calculated for 1/2s exposure times. Only the images of kidneys were obtained in exposure time of 1/12s, as the images at longer exposure times were oversaturated. It was confirmed that the images obtained in fluorescence microscope at different exposure times, after processing in ImageJ, gave the values that were in linear trend below Integrated Density value of 12000 (Figure 27- see “excluded value”). The exposure time of 1/12 s for the kidneys was chosen after visual assessment of obtained images. Also, the values obtained from ImageJ software at this exposure time were found in the linear range. Averaged intensities of the signal are presented in Figure 28 and 29 (i.v. and s.c. injection, respectively). Signal from the kidney is presented in Figure 30. The obtained values and calculated standard deviations are shown in Table 3.

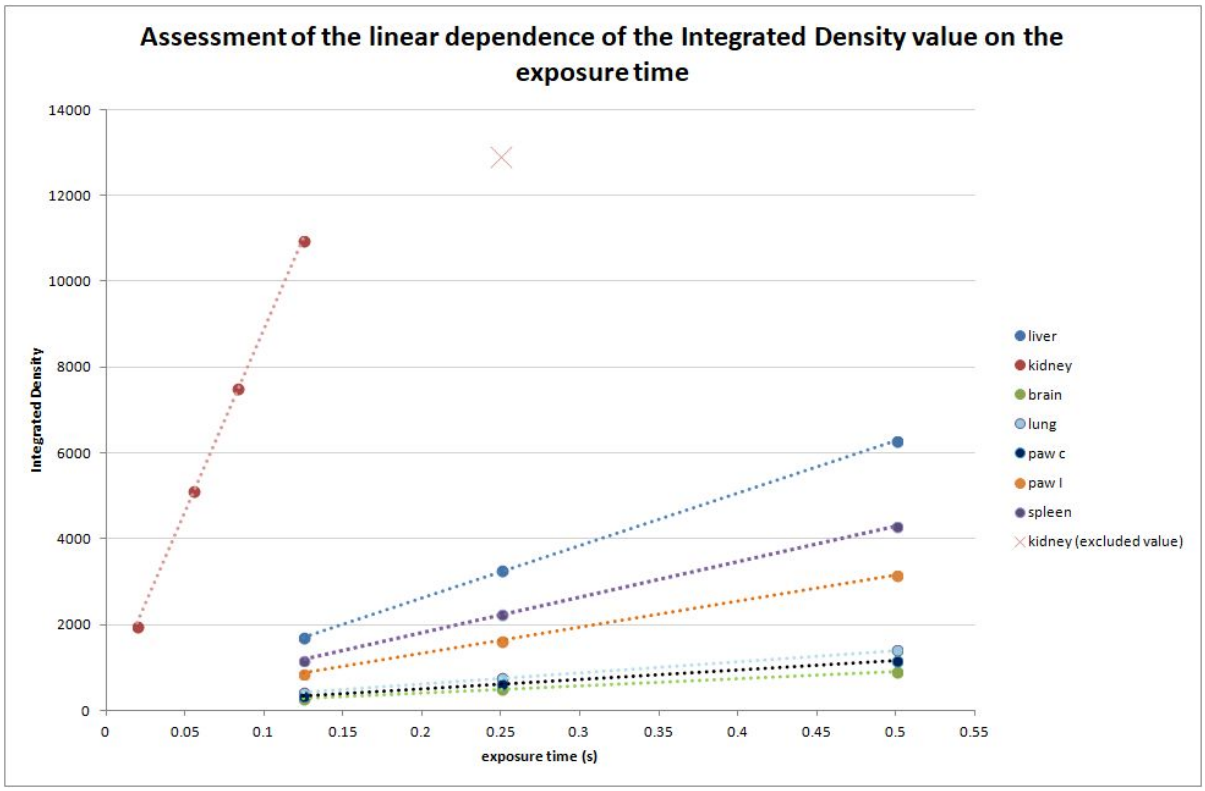


Figure 27: Diagram of dependence of the signal intensity (Integrated Density) on the exposure times. The values are in linear range below the value of 12000 (excluded point).

| | | hPG-Cy3-Succ-API (7%) | | hPG-Cy3-Succ-API (3.5%) | | hPG-Cy3-Succ | | hPG-Cy3 | | Cy3 | |
|---|---|---|---|---|---|---|---|---|---|---|---|
| type of injection | organ | normalized integrated density | st. dev | normalized integrated density | st. dev | normalized integrated density | st. dev | normalized integrated density | st. dev | normalized integrated density | st. dev |
| IV | brain | 129 | 46 | -114 | 10 | -14 | 28 | -27 | 7 | 126 | 74 |
| | liver | 5678 | 798 | 4144 | 790 | 3081 | 2526 | 2 | 96 | 141 | 93 |
| | lung | 823 | 237 | 146 | 27 | -8 | 36 | 192 | 54 | 240 | 106 |
| | paw C | 780 | 88 | 326 | 71 | 91 | 183 | 273 | 52 | 327 | 154 |
| | paw I | 1296 | 754 | 199 | 43 | 202 | 375 | 199 | 26 | 195 | 109 |
| | spleen | 3916 | 2033 | 1449 | 423 | 1787 | 2270 | 45 | 23 | 325 | 227 |
| | kidney (1/12) | 6782 | 718 | 1764 | 426 | 1176 | 1140 | 647 | 22 | 71 | 36 |
| SC | brain | 42 | 50 | -33 | 16 | -12 | 4 | -33 | 51 | 50 | 1 |
| | liver | 2045 | 409 | 1694 | 441 | 4556 | 1499 | -102 | 23 | 664 | 40 |
| | lung | 202 | 85 | 62 | 90 | 689 | 129 | 10 | 65 | 267 | 77 |
| | paw C | 254 | 104 | 100 | 86 | 460 | 61 | -26 | 61 | 286 | 160 |
| | paw I | 184 | 114 | 141 | 135 | 507 | 107 | -5 | 76 | 217 | 70 |
| | spleen | 845 | 237 | 538 | 75 | 1377 | 319 | 111 | 95 | 190 | 8 |
| | kidney (1/12) | 2076 | 937 | 2145 | 1315 | 636 | 156 | 267 | 122 | 92 | 16 |

Table 3: Normalized Integrated density values and standard deviations (st. dev) of the conjugates

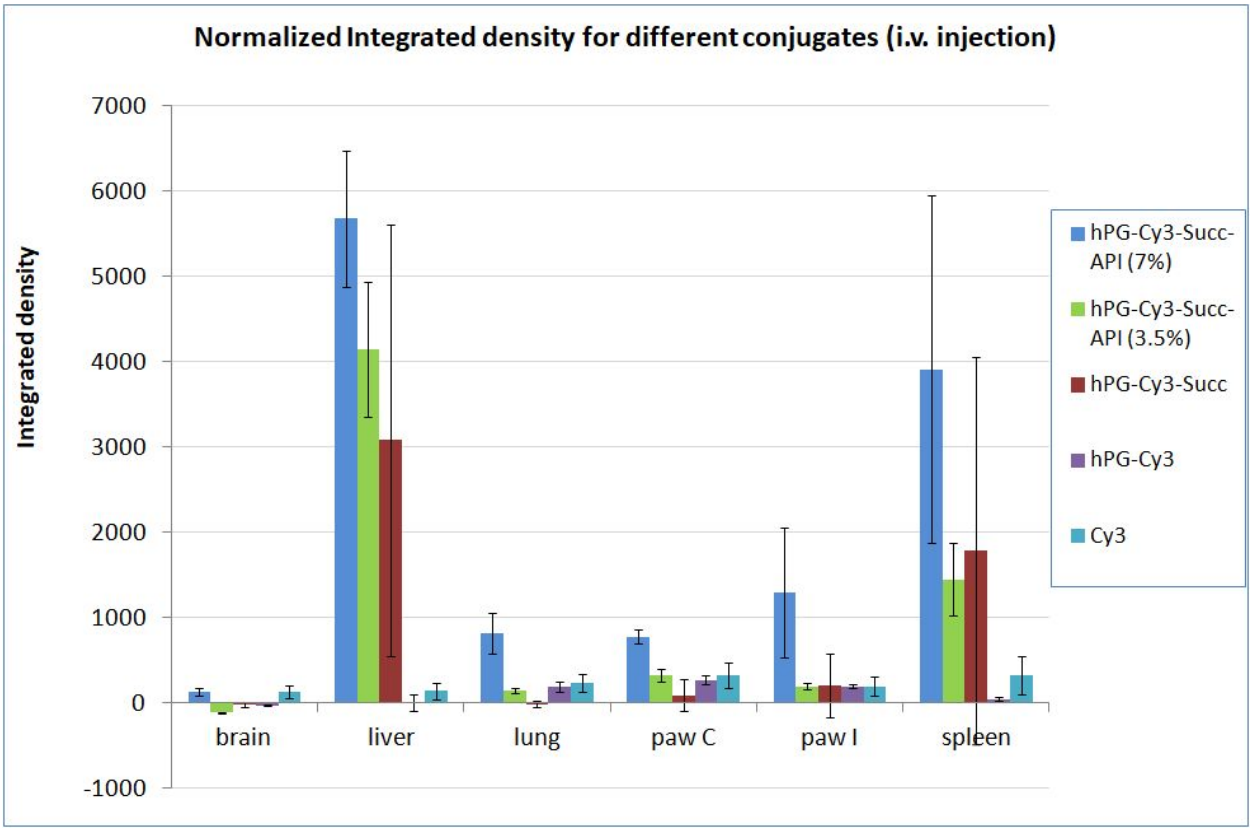


Figure 28: Relative intensities of the signals ingroups and different organs for i.v. injections. The values represent the averaged value of all computed images.

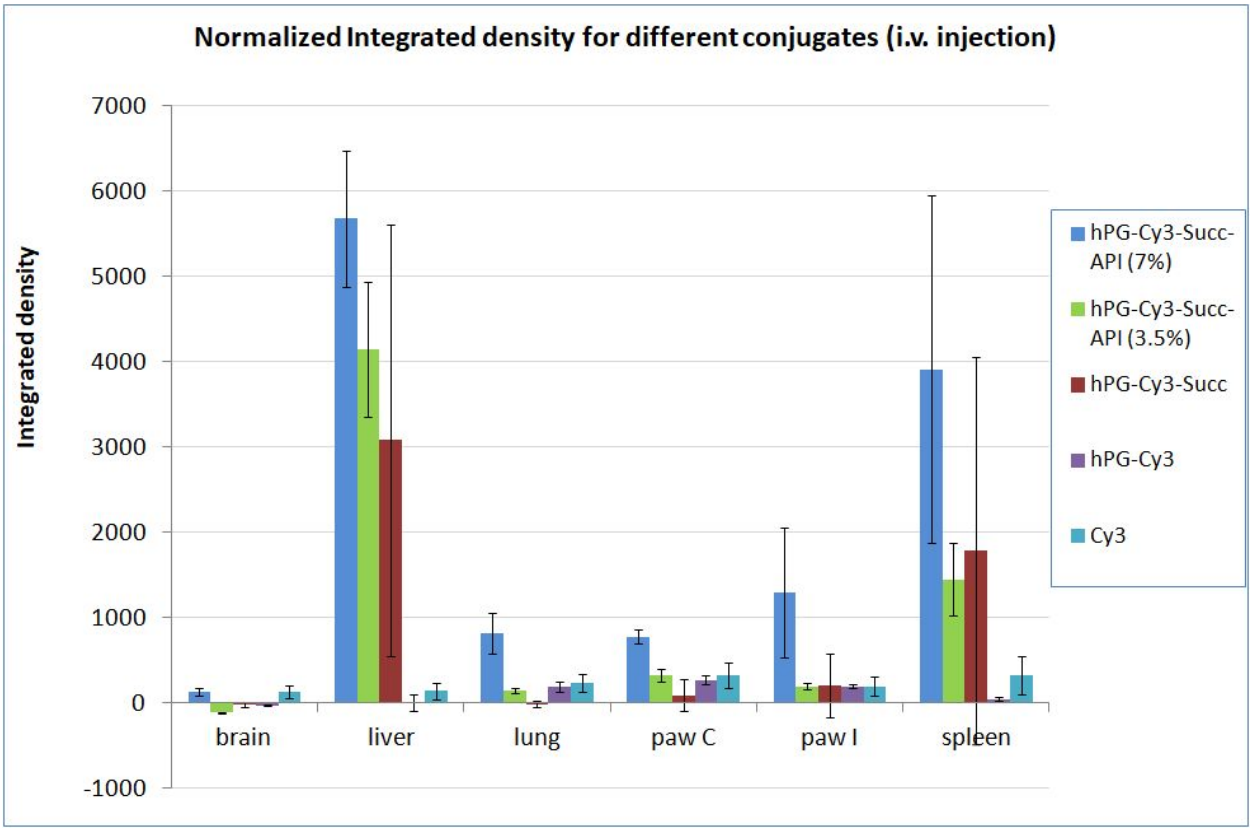


Figure 29: Relative intensities of the signals ingroups and different organs for s.c. injections. The values represent the averaged value of all computed images.

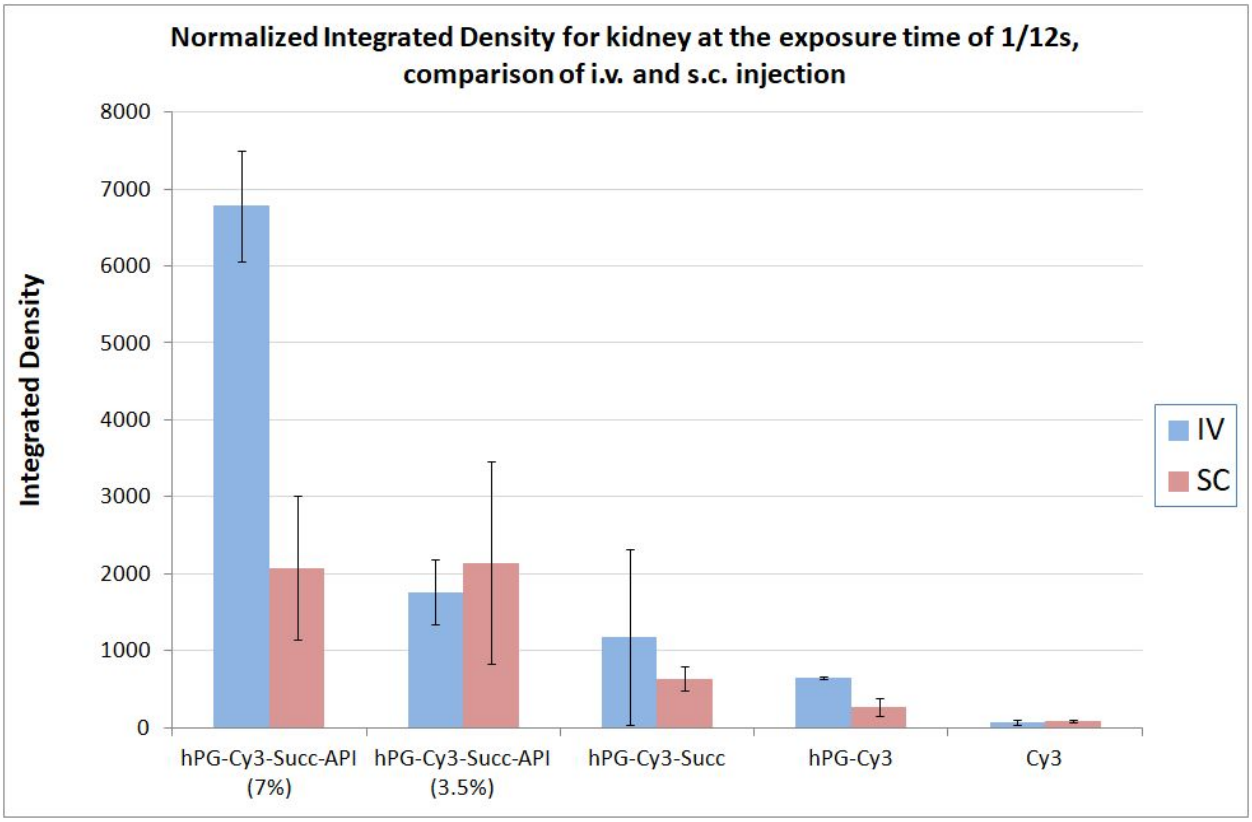


Figure 30.:Values of Integrated Density minus background signal from images of the kidney obtained at an exposure time of 1/12s.

The strength of the signal appears to be highest in the kidney, spleen and liver. In case of i.v. injections, hPG-Cy3-Succ-API 7% gives the highest values, whereas for s.c. injections there is a vantage of hPG-Cy3-Succ. The lowest signal in liver, spleen and kidney come from hPG-Cy3 and mere Cy3. Negative values in the brain (hPG-Cy3-Succ-API (3.5%), i.v. and s.c.), lung (hPG-Cy3-Succ, i.v.), liver (hPG-Cy3, s.c.) and paws (hPG-Cy3, s.c.) are most likely the result of the higher background in the control samples (no treatment). High standard deviations reflect high differences in signal intensities between the rats. For hPG-Cy3-Succ-API 7% i.v. and hPG-Cy3-Succ i.v., a slight advantage in the signal intensity in the inflamed paw (Paw I) can be observed, compared to non-inflamed paw (Paw C). For other constructs the difference in lung and both paws is low. In the kidney, the highest signal comes as well from hPG-Cy3-Succ-API 7% i.v., however in case of hPG-Cy3-Succ-API (3.5%), the values are higher in case of the s.c. injections. Nevertheless, it can be concluded that the intravenous injection gives an overall higher signal in the examined samples. The values obtained in this step were used for the estimation of the real concentration of the conjugates in the organs.

## 4.4. Calibration curve

To determine the concentration of the labelled constructs or mere dye in the organs, a series of dilutions of the dye was prepared from the initial concentration 1.078 mg/mL. The images were obtained at an exposure time of 1/2s and 1/12s and documented by means of fluorescence microscope. Subsequently the images were analysed by “imageJ” software. The dilutions measured are presented in Table 4. Additionally, a blank integrated density was calculated. After subtraction thereof from each of the integrated densities of each dilution image, two calibration curves were determined (Figure 31 and 32). The latter one was used for calculation of the concentration in kidney at an exposure time of 1/12s. From obtained calibration curves it was concluded that the detection limit is 2 µg/mL of the dye, as the Integrated Density values below this value lose the linear trend.

| Dye dilution | Normalized integrated density (exp. time 1/2s) | Normalized integrated density (exp. time 1/12s) | Corresponding concentration (µg/mL) |
|---|---|---|---|
| 1 : 64 | 10118.814 | 1885.173 | 16.844 |
| 1 : 128 | 7246.047 | 1412.011 | 8.422 |
| 1 : 256 | 2090.554 | 517.861 | 4.211 |
| 1 : 512 | 1154.747 | 373.432 | 2.105 |
| 1 : 1024 | 347.930 | 240.793 | 1.053 |
| 1 : 2048 | 324.008 | 240.227 | 0.526 |

Table 4. Integrated densities of the dye dilutions with corresponding known concentrations at an exposure time of 1/2s and 1/12s. The blank integrated density was subtracted from each value.

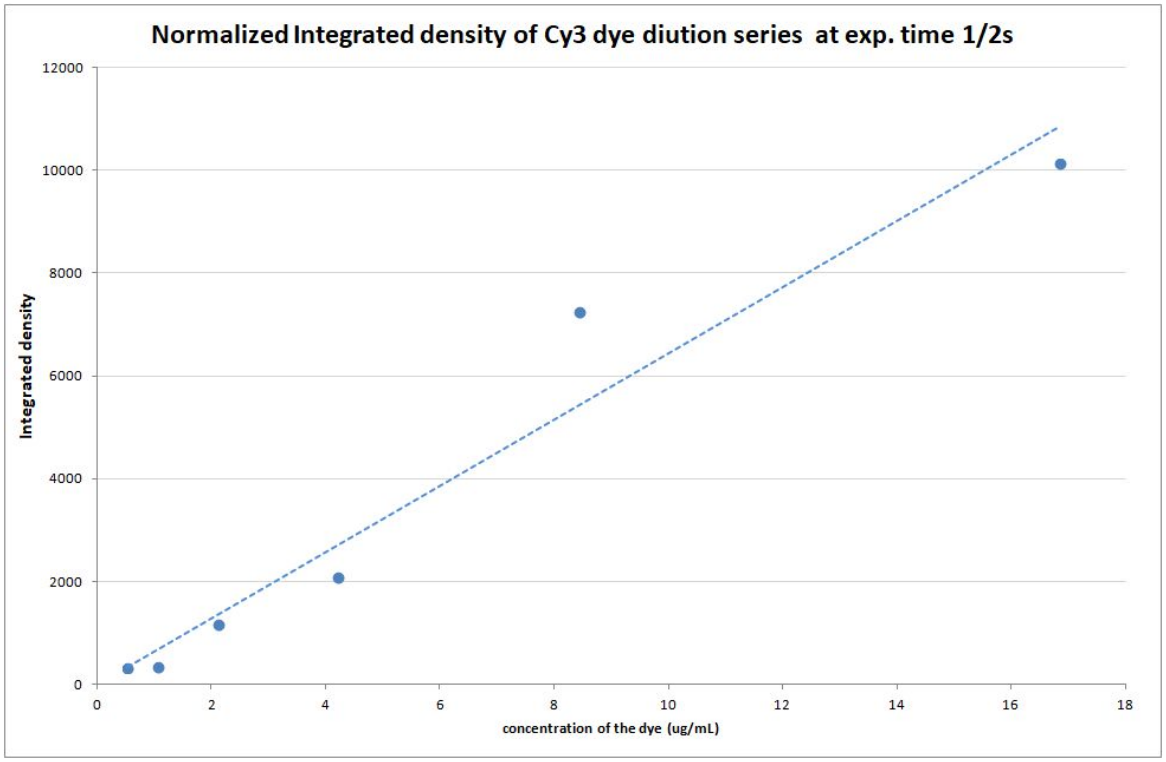


Figure 31. The calibration curve obtained from the Cy3 dilutions with known concentration, analysed by means of “ImageJ” software at an exposure time of 1/2s.

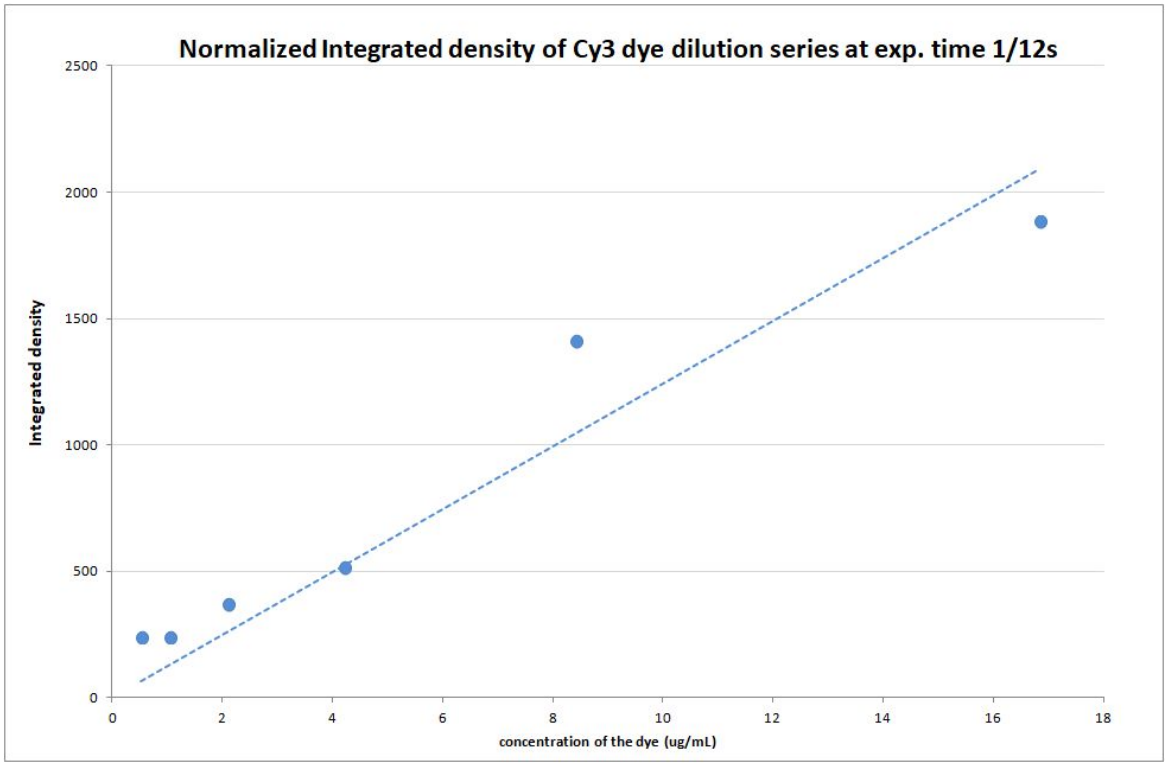


Figure 32. The calibration curve obtained from the Cy3 dilutions with known concentration, analysed by means of “ImageJ” software at an exposure time of 1/12s.

## 4.5. Estimation of real concentration of the conjugates

Obtained calibration curves were used to calculate the concentration of the dye within the tissues. Since degree of functionalization of the dye of every conjugate was known, this value was used to recalculate the concentration of the whole conjugate in each tissue, in each group (mg/mL) (see Materials and Methods section). After excluding the concentrations below the set limit of detection, the obtained concentrations of the conjugates are presented in Figure 33 and 34 (i.v. and s.c. injection, respectively). Calculated concentrations are presented in Table 5.

| | | hPG-Cy3-Succ-API (7%) | | hPG-Cy3-Succ-API (3.5%) | | hPG-Cy3-Succ | | hPG-Cy3 | |
|---|---|---|---|---|---|---|---|---|---|
| type of injection | organ | concentration (mg/mL) | st. dev | concentration (mg/mL) | st. dev | concentration (mg/mL) | st. dev | concentration (mg/mL) | st. dev |
| IV | brain | - | - | - | - | - | - | - | - |
| | liver | 0.7 | 0.1 | 0.41 | 0.08 | 0.16 | 0.13 | - | - |
| | lung | 0.1 | 0.03 | - | - | - | - | - | - |
| | paw C | 0.1 | 0.01 | - | - | - | - | - | - |
| | paw I | 0.16 | 0.09 | - | - | - | - | - | - |
| | spleen | 0.48 | 0.25 | 0.14 | 0.04 | 0.09 | 0.12 | - | - |
| | kidney | 4.3 | 0.45 | 0.91 | 0.22 | 0.31 | 0.31 | 0.14 | 0.004 |
| SC | brain | - | - | - | - | - | - | - | - |
| | liver | 0.25 | 0.05 | 0.17 | 0.04 | 0.24 | 0.08 | - | - |
| | lung | - | - | - | - | 0.04 | 0.01 | - | - |
| | paw C | - | - | - | - | - | 0 | - | - |
| | paw I | - | - | - | - | - | 0 | - | - |
| | spleen | 0.1 | 0.03 | - | - | 0.07 | 0.02 | - | - |
| | kidney | 1.32 | 0.59 | 1.1 | 0.68 | 0.17 | 0.04 | 0.06 | 0.03 |

Table 5: Calculated concentrations of the conjugates within the organs (mg/mL).

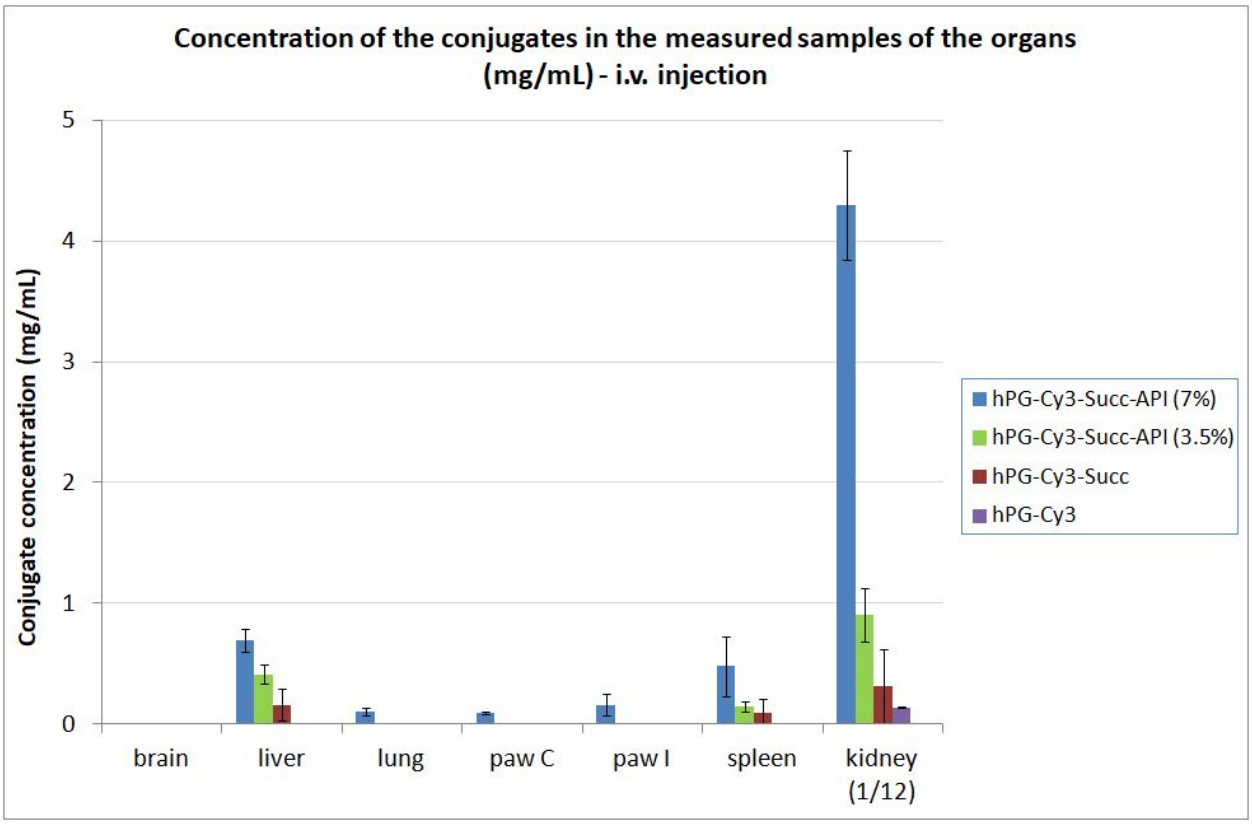


Figure 33: The estimated concentrations per mL of the whole conjugates, calculated by means of the computer software (ImageJ), excluding the values below the limit of detection (i.v. injections).

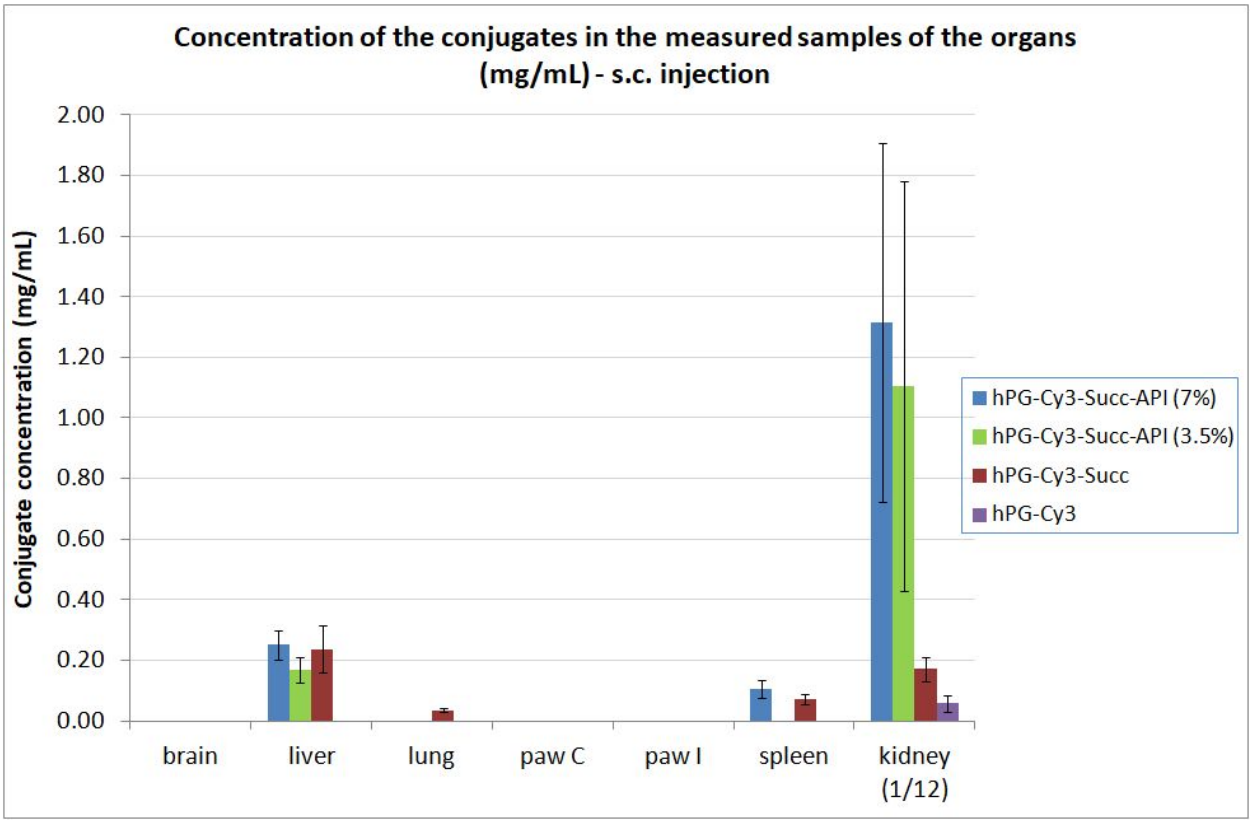


Figure 34: The estimated concentrations per mL of the whole conjugates, calculated by means of the computer software (ImageJ), excluding the values below the limit of detection (s.c. injections).

The i.v. injections gave higher concentrations. According to the calculated concentrations, this conjugate was present in every examined organ, apart from the brain. The results also show slightly higher concentrations in the inflamed paw, as compared to the non-inflamed one. Every conjugate considered as present in the tissue (above the limit of detection) has the highest concentration in the kidney. hPG-Cy3-Succ-API (7%) is present in ~5 times higher concentration in the kidney, than in the liver, which is the second organ having the highest concentration of the conjugate per mL. In case of hPG-Cy3-Succ-API (3.5%) and hPG-Cy3-Succ, the ratio between kidney and liver concentration is ~1:2. The latter two conjugates are yet only present in the kidney, spleen and liver. The hPG-Cy3 was only found in the kidney with the lowest concentration. The mere Cy3 dye was not detected in any examined group. In case of the s.c. injections the hPG-Cy3-Succ-API (7%) and hPG-Cy3-Succ-API (3.5%) were again found with the highest concentration in the kidney and the second highest concentration in the liver. This was however not true for the hPG-Cy3-Succ, where the concentration in the liver is ~30% higher, than in the kidney. Additionally, the hPG-Cy3-Succ

was also present in the lung, whereas other conjugates were not. According to the ImageJ analysis, no conjugate was present in neither inflamed, nor non-inflamed paw. Surprisingly, no hPG-Cy3-Succ-API (3.5%) was present in the spleen. The hPG-Cy3 was only found in the kidney with the lowest concentration. No mere Cy3 was detected in any organ of any group. In none of the examined groups, no signal was detected in the brain, regardless of the type of injection. Subsequent step of concentration estimation included referring obtained values to the volume of the whole organ examined. The organ volumes were taken from literature (see table 6). If the volume of an organ was described for rats with lower weight than used in this study, but given as a range of values, the highest value taken for the calculations. For the paws, the volume was estimated roughly after visual examination, considering that the inflamed paw was bigger by ~30% from the non-inflamed one.

| Organ | Volume (mL) | Reference |
|---|---|---|
| lung | 3.50 | [71] |
| kidney (both) | 3.00 | [72] |
| spleen | 1.00 | [72] |
| liver | 12.00 | [73] |
| paw I | 0.10 | Visual estimation |
| paw C | 0.07 | Visual estimation |

Table 6: Volumes of the rat organs according to the literature. For inflamed (paw I) and non-inflamed paw (paw C), the visual estimation helped to roughly estimate the volume of the tissue.

The average concentration of the conjugates in the organs were multiplied by the mean volume of the organs from Table 7. Obtained amounts of the conjugates per organ were compared with the dose injected (the dose for 350 g rat, the average weight out of rat weights used in this study), to define the percentage of the dose that was distributed within the organs. The amount of the compounds and percentage fractions are presented in Table 5. The results show the distribution percentage exceeding the initial dose injected, even up to 347% in case of i.v. injected hPG-Cy3-Succ-API (7%). These values are lower than 100% only for the hPG-Cy3 conjugate. For hPG-Cy3-Succ-API (7%), hPG-Cy3-Succ-API (3.5%) and hPG-Cy3, the intravenous injection show higher content of the conjugates than in subcutaneous injected

groups. The gathered data however show different pattern for hPG-Cy3-Succ conjugate. Only in this case the content of the conjugate is higher in s.c. injected group, however the difference is also the smallest, when compared to the differences between injection types in other groups.

| | | amount of conjugate per organ (mg) | | | |
|---|---|---|---|---|---|
| Injection type | organ | hPG-Cy3-Succ-API (7%) | hPG-Cy3-Succ-API (3.5%) | hPG-Cy3-Succ | hPG-Cy3 |
| i.v. | liver | 8.34 | 4.94 | 1.91 | - |
| | lung | 0.35 | - | - | - |
| | paw C | 0.01 | - | - | - |
| | paw I | 0.02 | - | - | - |
| | spleen | 0.48 | 0.14 | 0.09 | - |
| | kidney | 12.89 | 2.72 | 0.94 | 0.42 |
| | sum | 22.08 | 7.81 | 2.95 | 0.42 |
| | dose injected (mg) | 6.36 | 5.17 | 2.69 | 2.17 |
| | % fraction | **347%** | **151%** | **110%** | **19%** |
| s.c. | liver | 3.00 | 2.02 | 2.83 | - |
| | lung | - | - | 0.12 | - |
| | paw C | - | - | - | - |
| | paw I | - | - | - | - |
| | spleen | 0.10 | - | 0.07 | - |
| | kidney | 3.95 | 3.31 | 0.51 | 0.17 |
| | sum | 7.05 | 5.33 | 3.53 | 0.17 |
| | dose injected (mg) | 6.36 | 5.17 | 2.69 | 2.17 |
| | % fraction | **111%** | **103%** | **131%** | **8%** |

Table 7: Averaged amounts of the conjugate in particular organs and their percentage fractions of the injected dose into 350 g rat, which was the average weight of the animals used in this study.

## 4.6. Assessment of the spatial correlation between the cells nuclei and conjugate signal.

DAPI binds exclusively to DNA, therefore by using this staining agent, it is possible to visualize the nuclei of the cells within the tissue. Combining it together with Cy3-labeling of the construct, it is possible to check, whether there is a certain pattern of the distribution of the conjugate. The conjugates, which were observed in the visual assessment (hPG-Cy3-Succ-API 7% and 3.5%, hPG-Cy3-Succ) are considered to behave in a similar manner. Examples of the spatial correlation between the nuclei and the conjugates are presented in the Figure 35.

In kidney the signal from the conjugates omits the cells, but rather appear in the places, where very few or no nuclei were present (Figure 35 C).

In liver, the signal from the conjugates were found in a position closely related to the stained nuclei (Figure 35 F) and seem to be evenly distributed throughout the tissue.

In the lung, the signal is also related to the nuclei, however in this case the signal occurs in less distributed manner, but more like correlated with only a few cells (Figure 35 I).

This is also true for the inflamed paw, however in this tissue, the nuclei aggregation in one particular site could be observer and the signal was strongly correlated with this site (Figure 35 L).

A similar pattern was noticed for the spleen, where the conjugates were present in the cavities with no or very few stained nuclei (Figure 35 O).

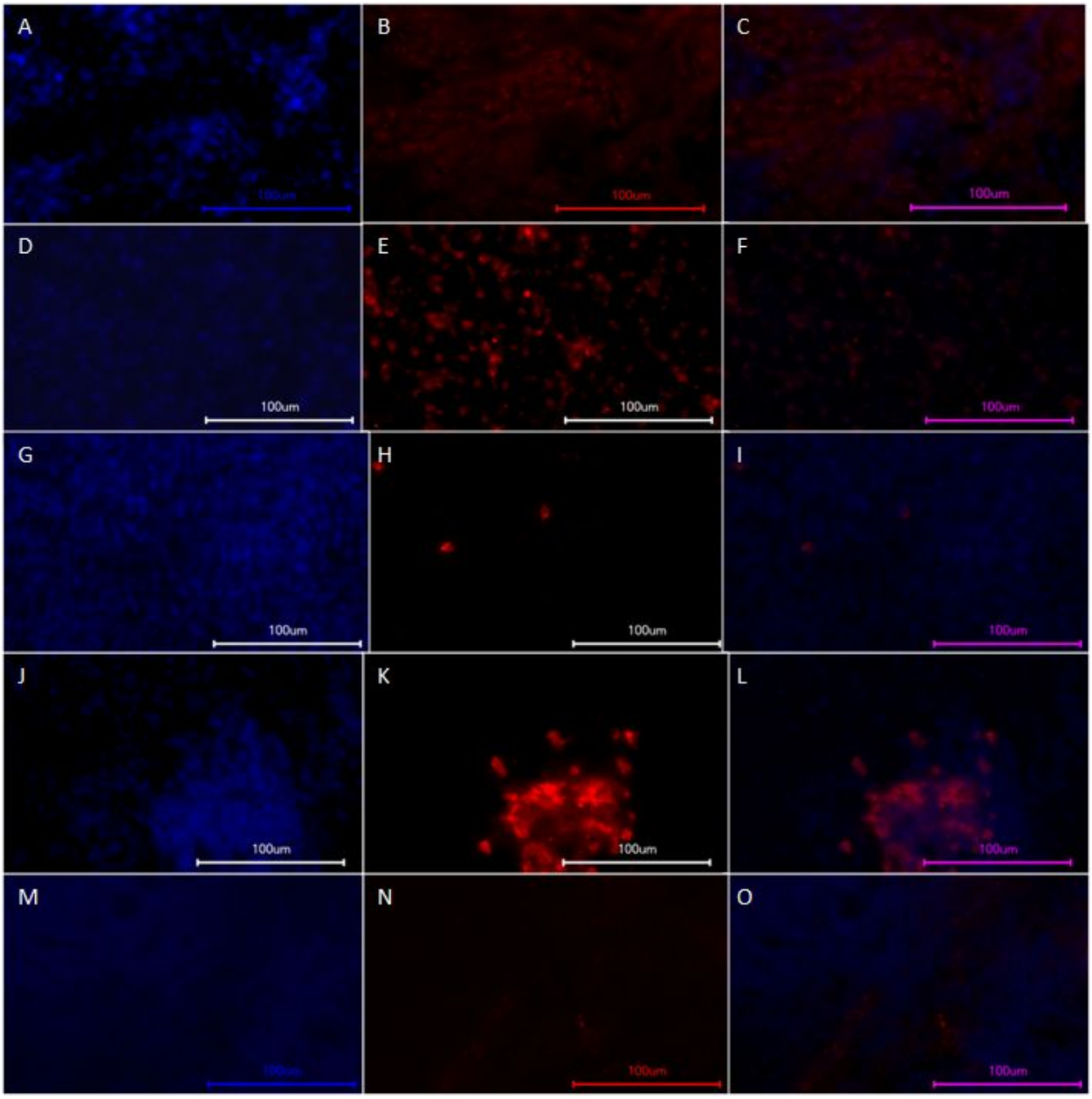


Figure 35: Left column represents the DAPI signal coming from the stained nuclei. Middle column shows the Cy3 labeled conjugates. Right column shows the overlayed images. A-C: kidney (hPG-Cy3-Succ, i.v.); D-F: liver (hPG-Cy3-Succ-API (7%), i.v.); G-I: lung (hPG-Cy3-Succ-API (7%), i.v.); J-L: paw I (hPG-Cy3-Succ, s.c.); M-O; spleen (hPG-Cy3-Succ, i.v.). Scale bar: 100 µm.

## 4.7. Spectrofluorometry

Spectrofluorimetry of the treated rats was performed. Excitation wavelength was 555nm, the emission peak appeared at 570 nm, which corresponds to the fluorescence of the Cy3 dye. Calibration curves were obtained by measuring a series of dilutions of the hPG-Cy3 and hPG-Cy3-Succ with known concentration. To provide the same environment of the standard samples and urine samples, the conjugates were initially dissolved in rats urine and subsequently diluted with PBS. The urine sample were also diluted in PBS. The obtained calibration curves are presented in Figure 36 and 37 (hPG-Cy3 and hPG-Cy3-Succ, respectively). Weight of all rats was in range 345-355 g and the collected urine was 2 mL and 4 mL in volume in rats treated with hPG-Cy3 (after 2h and 6h respectively). In case of hPG-Cy3-Succ treated rats, the urine volumes were 1.5 mL and 3 mL (after 2h and 6h, respectively). Examples of the obtained spectra are presented in Figure 38 and 39.

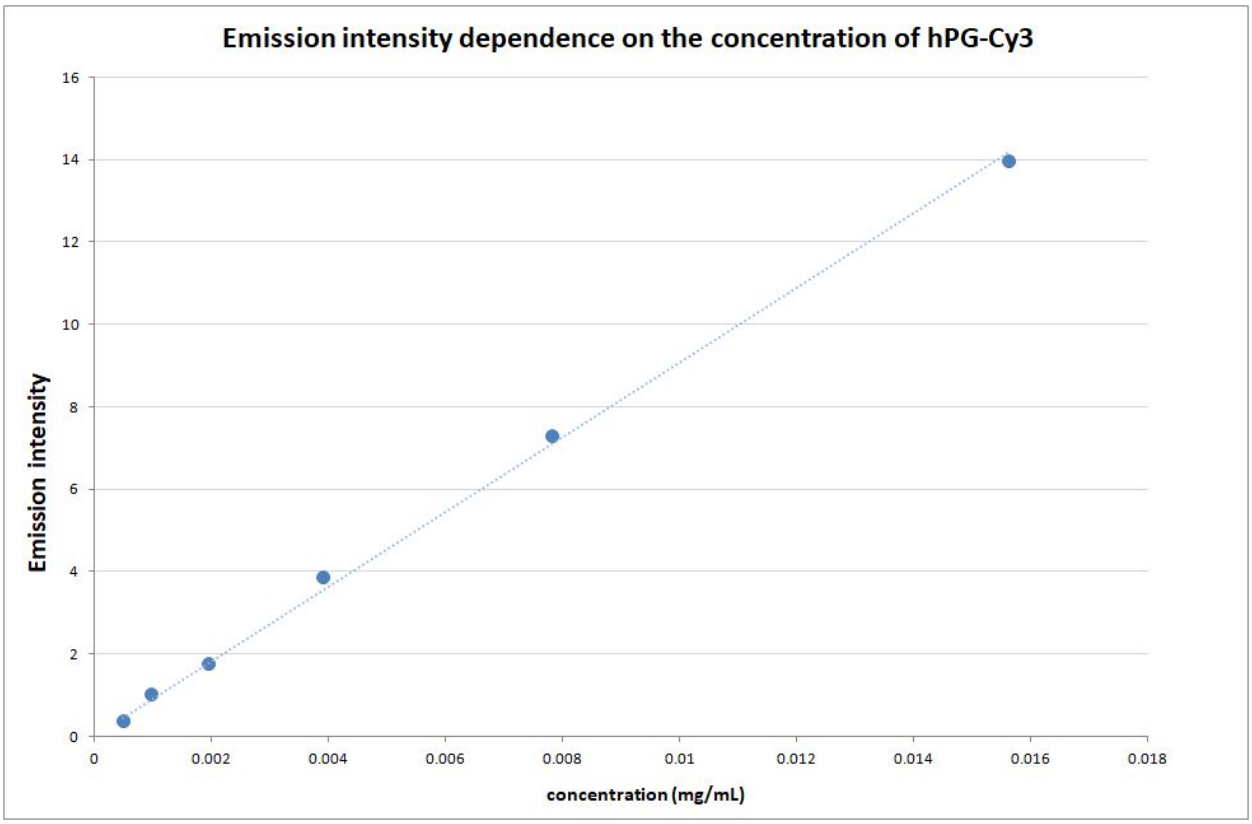


Figure 36: Calibration curve obtained for the hPG-Cy3 conjugate

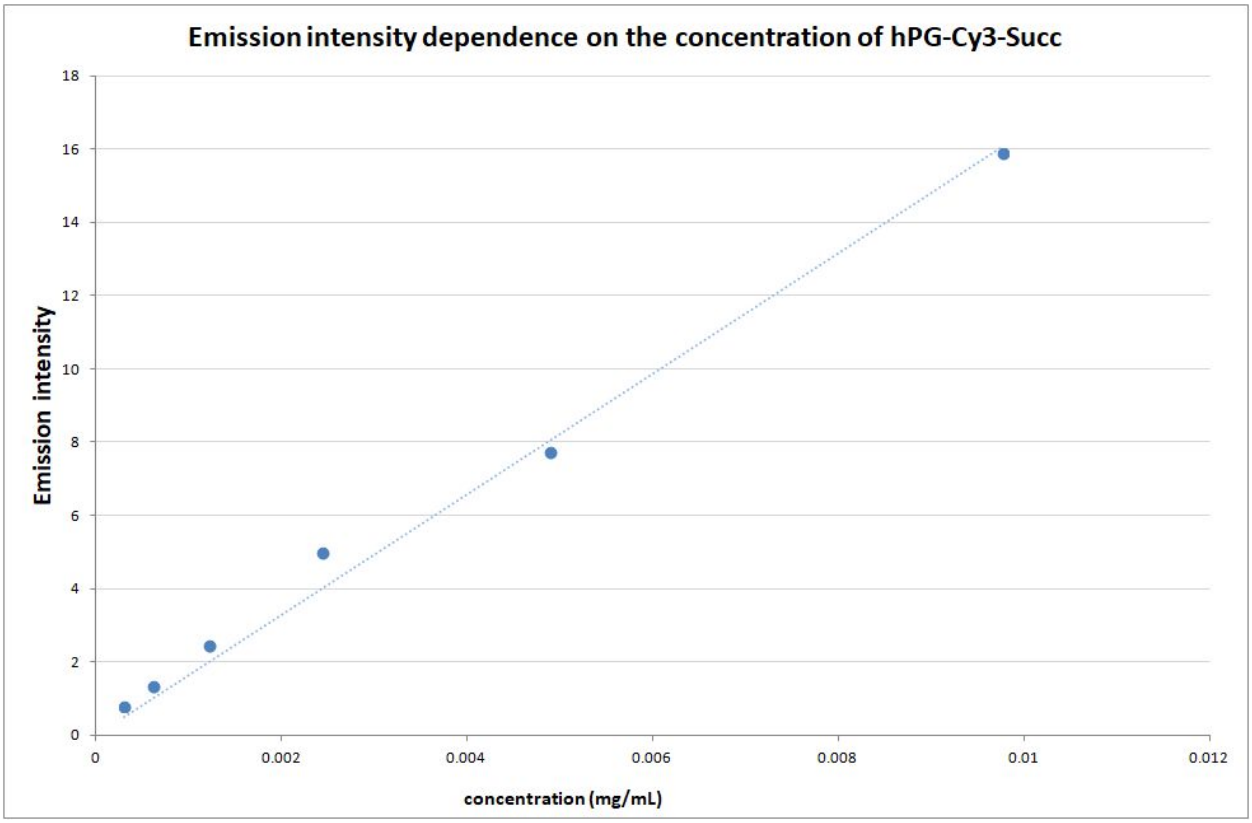


Figure 37: Calibration curve obtained for the hPG-Cy3-Succ conjugate.

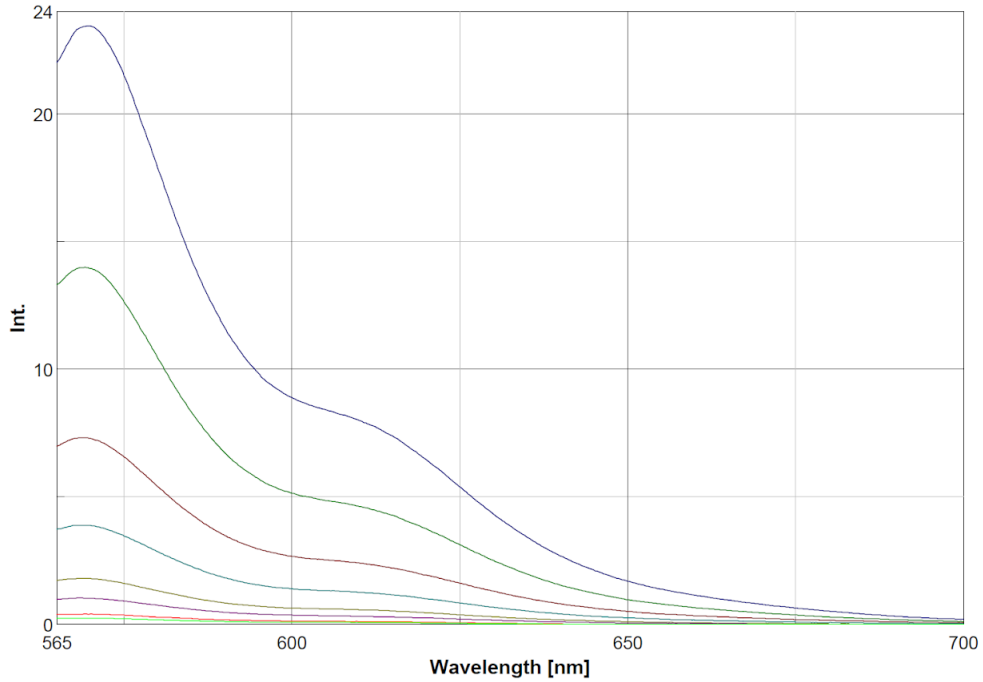


Figure 38: Emission spectra of the diluted samples of hPG-Cy3 used for the calibration curve.

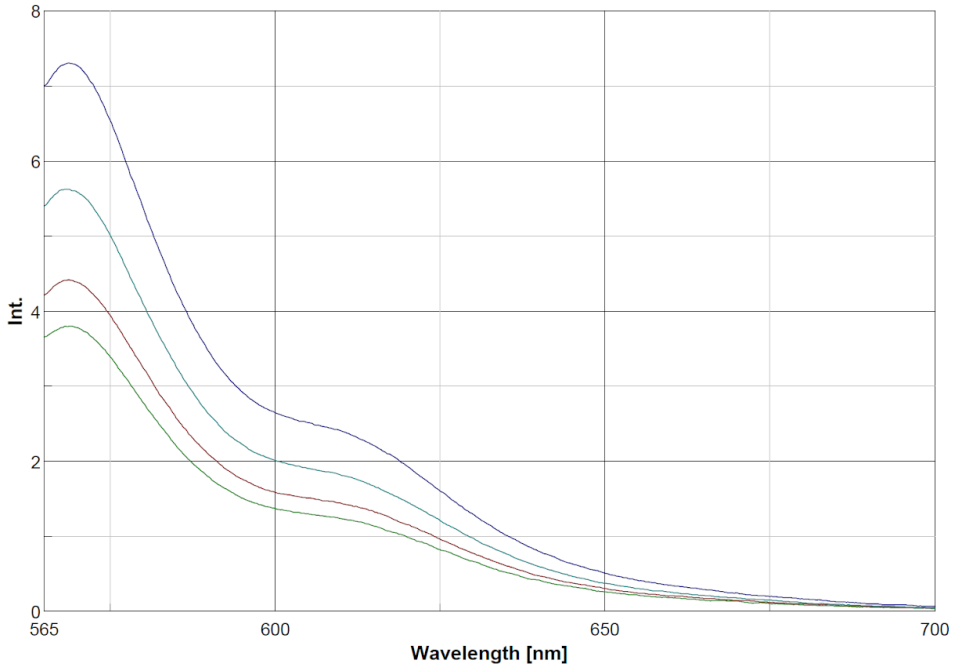


Figure 39: Example emission spectra of the urine containing hPG-Cy3 after 2h.

From the calibration curve, the calculated concentration of the conjugates were 0.74 mg/mL and 0.45 mg/mL for hPG-Cy3 (after 2h and 6h, respectively), which corresponds to 51% and 62% of excreted hPG-Cy3 after 2h and 6h, respectively. Concentration of hPG-Cy3-Succ was found to be 0.32 mg/mL and 0.17 mg/mL after 2h and 6h, respectively. Those concentrations correspond to 7% and 8% of the excreted conjugate after 2h and 6h respectively.

# 5. Discussion

The study on the biodistribution of the polymer-based Cy3-labelled conjugates in rats *in vivo* was performed. Quantitative analysis of each conjugate within the organs was assessed by means of fluorescence microscopy with respect to the calibration curve prepared from the dilutions of mere Cy3 dye. The qualitative examination of the tissues along side to the quantitative method was done. From obtained data it was possible to gain some insight in the behaviour of the examined nanoparticles 60 min after injection.

Firstly, from the obtained relative intensities and recalculated concentrations of the conjugates it became clear, that after subcutaneous injection lower amounts of the conjugates were found in tissues compared to intravenous injection. This stands with agreement with the examples found in the literature. It is generally stated that the bioavailability of the compound injected s.c. can vary from 12% to 100% [74] as compared to 100% by definition. It was also

noted that the absorption of particles injected via this route is extended over time and the bioavailability depends on the site of injection [75]. Perhaps examination organs at different time points would show whether the concentration of the conjugates is increasing. In this study the desired site of s.c. was in abdominum, however in some cases the injection was made in subcutis of the tail. The difference in biodistribution due to two different sites of injection was not examined in this research. In contrast, conjugates injected intravenously instantly had 100% of the compound in the systemic circulation. The two exceptions to this pattern were the s.c. injected hPG-Cy3-Succ found in the liver in higher amount that in case of i.v. injected rats (0.14 mg/mL vs 0.41 mg/mL) and generally found in the lung, where is was absent in case of i.v. injections. Also in case of hPG-Cy3-Succ-API (3.5%) the s.c. injection gave higher signal in the kidney compared to i.v. (1.1 mg/mL and 0.91 mg/mL, respectively). The reason for this observation is considered as a result of different amounts of examined rats in each group. This matter and the high standard deviations are going to be discussed later.

When comparing the quantitative results of the conjugates distribution with the quantitative assessment a few discrepancies are to be observed. Mostly the fact that according to the computational method, the conjugates were to be found only in the inflamed paw (Paw I) in case of hPG-Cy3-Succ-API (7%)-i.v., whereas it was also noticed visually in hPG-Cy3-Succ (i.v.) treated rats, as well as in hPG-Cy3-Succ-API (3.5%) (i.v.), yet to smaller extent. The imageJ software was used to calculate the Integrated Density, which is a Mean Gray value of the pixels multiplied by the analyzed area within the image (pixel values may vary from 0 to 255, referring to black and white color, respectively). For normalization of the results the analyzed area was the whole image (all images had the same number of pixels). Therefore, the signal which was aggregated in case of the paws was lost within the majority of “black” pixels (lower range of pixel values). On the other hand, the presence of the signal in the control paw is unexpected. Indeed, the software gave the values, which overall gave the intensity considered to be above the detection limit, yet the signal is considered to be non specific, as it only reflected the histological structure of the tissue and thus was considered as a background signal. This pattern of “highlighting” the structure repeated also for other organs, mostly for the liver and the kidney. The idea of this quantitative analysis was to subtract the background signal from each image to obtain the real intensity values within the examined species. However in most of the cases, the background in the images bearing the labelled conjugate, was higher than the background of the control samples, but this is true only for the conjugates considered qualitatively as positive (both hPG-Cy3-Succ-APIs and hPG-Cy3-Succ). In case of mere Cy3

dye, where no signal was detected, the overall color of the image was black. It is therefore hypothesized that the reason for this behaviour was a poorly performed perfusion, which resulted from the signal from the Cy3-labelled conjugates distributed within the tissue (internalized into cells) and from the remaining blood (bearing fluorescent moiety). This can be somewhat confirmed due to the fact, that Cy3 images were black, meaning the lack of the signal, which would suggest the rapid and full excretion of the substance from the blood circulation (most likely rapid renal excretion). This is possible as the MW of Cy3 is 664, whereas the renal molecular cut off is 80 000 Da [76]. Moreover, the wavelength used for the Cy3 excitation was ~540 nm and the emission filter cut-off was ~590 nm. No autofluorescence occurs in tissues upon excitation with this wavelength (blue and UV light is responsible for the autofluorescence in tissues) [77].

The signal of hPG-Cy3 was only found in the kidney and was weaker to other conjugates, which suggests that the clearance pathway is mostly renal and that and that the opsonization and action of the MPS is not significant for this conjugate.

Quantitative results obtained by means of fluorescence microscopy suggest that the amount of the conjugates injected exceeded the amount injected (apart from hPG-Cy3). This can be again referred to the high background signal, which could result from the blood residues but also from the type of microscopy used in this research. The conventional fluorescence microscopy, which was used in this study, collects the emitted light from the focal plane, but also from the out-of-focus site, which is from above and below the focal plane [78]. The emitted non-specific signal contributes to an overall intensity of the signal within the image. To overcome this problem, the dye dilutions used for the calibration curve were applied on the microscopy slide in volume, that should give the same thickness as the specimen, therefore the out-of-focus signal should be incorporated into the calibration curve equation. Nevertheless, different microscopy technique might have given more accurate results. For example Laser Scanning Confocal Microscopy (CLSM), which excludes the out-of-focus signal by letting only the in-focus light to travel through the pinhole to the detector [79].

Lastly, it has been reported, that Cy3 dye bound to large molecule can hinder the cis-trans izomerization, i.e. a photoinduced effect in which the fluorophore in the excited state comes back to thermodynamic equilibrium. Preventing this conversion results in higher quantum yield of the complex (dye-molecule) compared to the mere dye [80]. Referring the obtained results to the calibration curve made from the same complex as measured (not just the mere dye) would probably verify this issue.

High standard deviations in the obtained results were expected due to the individual differences between the rats and their physiological response to the environment, for example to the stress [81].

It is relevant to have a representative number of individuals in each group. According to OECD (Organization for Co-Operation and Development), at least 4 rat of one sex should be tested for each dose, where i.v. and s.c. should be considered independently [82]. In this research, the number of rats varies in different groups and therefore makes the quantitative analysis more prone to high deviations. To supplement the statistical input, at least 4 images of each organ were measured, however it was mainly meant to average a signal intensity throughout the organ and did not cover the differences between individuals. The research to be conducted in the future should include more (at least 4) animals per one group to obtain more accurate results.

It was expected that renal clearance will be a preferential elimination pathway, and this prediction was successfully reflected in the results, in both visual and software analysis. As mentioned before, the molecular cut-off of glomerular endothelium is around 80 kDa. The molecular weight of the biggest conjugate (hPG-Cy3-Succ-API 7%) was <28 kDa. No signal from Cy3 in any organ also suggests rapid clearance through the kidney. On the other hand the signal in the liver and spleen also stands in line with the findings in literature and is most likely due to the uptake by the cells of the MPS and in liver hepatocytes [83]. However, because of the relatively small size of the individual conjugate particle, it is hypothesized that the uptake was due to increased hydrodynamic radius of the formed agglomerates. This fact can be related to the zwitterionic character of the API-loaded conjugates, as the bound drug contains the tertiary amine which is in protonated state in the pH < 9 (physiological pH = 7.4). This can effect in attractive forces between the carboxylic groups of succinate and the amine groups of the drug in adjacent particles. However, it cannot be referred to the hPG-Cy3-Succ, which does not possess the amine groups and exhibits fully negative charge, and therefore the repulsions between the adjacent succinate chains are expected. However it is documented, that the plasma proteins bind non-specifically to nanoparticles after the reach the systemic circulation, which result with arising of protein corona, which can cause aggregation and increase in overall hydrodynamic radius [84]. Furthermore the protein corona can be recognized by the scavenger receptors of macrophages which facilitate the phagocytosis [85]. Since the biggest population of macrophages is present in the lung and liver, the signal from the lung can also be explained by the interactions with alveolar macrophages in the lung. Those potential aggregates can also be filtered in the red pulp of the spleen and internalized within the red pulp macrophages[86].

The positive signal in the inflamed paw was expected due to the passive targeting referred to the EPR effect. The agglomeration of cells recognized by the DAPI staining of the nuclei suggest the diffusion of the macrophages from the lymph nodes upon inflammation and the Cy3 fluorescent signal overlay is considered to occur due to the phagocytic activity thereof in the site of inflammation [87].

Low signal from the kidney and no signal from other organs from hPG-Cy3-treated rats can be attributed to the fact of lower molecular weight of the conjugate, as well as low affinity to the plasma proteins. It has been documented that due to high hydrophilicity and neutral charge, this polymer can be efficiently used as a coating for nanoparticles in order to escape the proteins in the blood and the MPS cells and can even outperform the PEG coating, which so far is considered to be the gold standard in preventing nanoparticles from the MPS uptake [88]. A plasma protein binding assay could help to fully confirm this hypothesis.

No signal was detected in the brain in any examined case. The blood-brain barrier (BBB) seems to be non-permeable for the examined conjugates and for the mere Cy3 dye. This is an expected result, as the BBB does not facilitate the transport of hydrophilic compounds (unless they contain ligand for the membrane transporters), whereas all of the conjugates (and the dye) are readily soluble in water. This feature is advantageous in the case of drug delivery of the drugs that can cause addictions when enter the central nervous system (CNS), for example opiate-based drugs in pain treatment. It has been documented that conjugation of morphine with hPG core via ester linker prevented the otherwise lipophilic (and BBB-permeable) morphine to cross the BBB. However, upon the hydrolysis of the ester bond (due to lower pH or increased enzymatic activity), it showed peripheral activity, and effective relief in pain. Therefore, that designed drug delivery system could prove efficient in treating the severe pain and decrease side effects, like addiction and abusive overdosing [89].

The spectrofluorimetry analysis of the urine obtained from the rats treated with i.v. injected hPG-Cy3 and hPG-Cy3-Succ gave results which stand in agreement with expectations and visual assessment of the organs. The rats treated with the hPG-Cy3 conjugate showed signal only in the kidney, and no signal in the liver, nor the spleen, which suggest that the renal clearance pathway is superior for this conjugate. This was confirmed by spectroscopic analysis, as over 50% of the conjugate was excreted after 2h after injection. Considering that hPG is the last remaining moiety after the hydrolysis of the ester bonds and releasing the API, the high clearance rate is promising and suggest, that most probably no accumulation in the organs occur. In contrast, the rats treated with hPG-Cy3-Succ showed signal in the spleen and the liver,

which suggest the involvement of MPS system in retaining the conjugate, but also the liver signal indicates that the hepatic clearance also takes place. However, low rates of excretion of hPG-Cy3-Succ can occur due to the accumulation of the conjugate in the organs which can later cause undesired toxic effects. To clarify the clearance rate, more time points should be implied and urine samples analysed. Additionally, the analysis of the blood serum and feces could put more light in to the retention and clearance of the conjugate.

# Conclusion and outlook

Nanocarriers based on the hPG polymer were examined *in vivo*. The carriers were found mostly in the liver, spleen and kidney. Renal clearance seems to be a preferential pathway of elimination. By visual assessment in the fluorescence microscope, the EPR effect was confirmed, as the signal was found in the inflamed paw, whereas no signal was observed in the non-inflamed paw, which suggests a site-specific targeting. However the quantitative analysis by means of fluorescence microscope gave too high values which is attributed to the contribution of the signal from the outside of the focal plane. However, the spectrofluorimetry gave reliable values of the concentration of conjugate in urine, which match the expectations and other collected data. Conjugation of the carriers with the fluorescent Cy3 dye proved to be useful in terms of tracing the compounds in the tissues.

To gain deeper insight in the real distribution of the conjugates, bigger number of time points would be useful to examine the distribution of the conjugates over time and calculate the clearance rate of the conjugates.

The BBB is impermeable for the presented conjugates, which makes them a promising candidate for the delivery of the drugs, which can cause side effects upon the interaction with the CNS. This architecture could be used in opiate-based formulations for treating severe pain without the induction of addiction.

[1] R. A. Copeland, ‘Evaluation of enzyme inhibitors in drug discovery. A guide for medicinal chemists and pharmacologists’, *Methods Biochem. Anal.*, vol. 46, pp. 1–265, 2005.
[2] J. Fan and I. A. M. de Lannoy, ‘Pharmacokinetics’, *Biochem. Pharmacol.*, vol. 87, no. 1, pp. 93–120, Jan. 2014.
[3] R. G. Strickley, ‘Solubilizing excipients in oral and injectable formulations’, *Pharm. Res.*, vol. 21, no. 2, pp. 201–230, Feb. 2004.
[4] S. A. Charman, C. S. Perry, F. C. K. Chiu, K. A. McIntosh, R. J. Prankerd, and W. N. Charman, ‘Alteration of the intravenous pharmacokinetics of a synthetic ozonide antimalarial in the presence of a modified cyclodextrin’, *J. Pharm. Sci.*, vol. 95, no. 2, pp. 256–267, Feb. 2006.
[5] R. P. J. Oude Elferink and R. de Waart, ‘Transporters in the intestine limiting drug and toxin absorption’, *J. Physiol. Biochem.*, vol. 63, no. 1, pp. 75–81, Mar. 2007.
[6] A. M. Butt, H. C. Jones, and N. J. Abbott, ‘Electrical resistance across the blood-brain barrier in anaesthetized rats: a developmental study.’, *J. Physiol.*, vol. 429, pp. 47–62, Oct. 1990.
[7] P. R. Lockman, R. J. Mumper, M. A. Khan, and D. D. Allen, ‘Nanoparticle technology for drug delivery across the blood-brain barrier’, *Drug Dev. Ind. Pharm.*, vol. 28, no. 1, pp. 1–13, Jan. 2002.
[8] W. W. Weber, ‘Protein binding’, *Adv. Biol. Skin*, vol. 12, pp. 61–63, 1972.
[9] K. J. Fehske, W. E. Müller, and U. Wollert, ‘The location of drug binding sites in human serum albumin’, *Biochem. Pharmacol.*, vol. 30, no. 7, pp. 687–692, Apr. 1981.
[10] K. C. Beaumont, A. G. Causey, P. E. Coates, and D. A. Smith, ‘Pharmacokinetics and metabolism of zamifenacin in mouse, rat, dog and man’, *Xenobiotica Fate Foreign Compd. Biol. Syst.*, vol. 26, no. 4, pp. 459–471, Apr. 1996.
[11] B. Meunier, S. P. de Visser, and S. Shaik, ‘Mechanism of oxidation reactions catalyzed by cytochrome p450 enzymes’, *Chem. Rev.*, vol. 104, no. 9, pp. 3947–3980, Sep. 2004.
[12] J. Belcher *et al.*, ‘Structure and Biochemical Properties of the Alkene Producing Cytochrome P450 OleTJE (CYP152L1) from the Jeotgalicoccus sp. 8456 Bacterium’, *J. Biol. Chem.*, vol. 289, no. 10, pp. 6535–6550, Mar. 2014.
[13] B. Wu, ‘Pharmacokinetic interplay of phase II metabolism and transport: a theoretical study’, *J. Pharm. Sci.*, vol. 101, no. 1, pp. 381–393, Jan. 2012.
[14] R. Nagashima, R. A. O’Reilly, and G. Levy, ‘Kinetics of pharmacologic effects in man: the anticoagulant action of warfarin’, *Clin. Pharmacol. Ther.*, vol. 10, no. 1, pp. 22–35, Feb. 1969.
[15] J. Mordenti, ‘Forecasting cephalosporin and monobactam antibiotic half-lives in humans from data collected in laboratory animals.’, *Antimicrob. Agents Chemother.*, vol. 27, no. 6, pp. 887–891, Jun. 1985.
[16] M. Longmire, P. L. Choyke, and H. Kobayashi, ‘Clearance properties of nano-sized particles and molecules as imaging agents: considerations and caveats’, *Nanomed.*, vol. 3, no. 5, pp. 703–717, Oct. 2008.
[17] T. Barrett, P. L. Choyke, and H. Kobayashi, ‘Imaging of the lymphatic system: new horizons’, *Contrast Media Mol. Imaging*, vol. 1, no. 6, pp. 230–245, Dec. 2006.
[18] S.-T. Yang *et al.*, ‘Covalently PEGylated carbon nanotubes with stealth character in vivo’, *Small Weinh. Bergstr. Ger.*, vol. 4, no. 7, pp. 940–944, Jul. 2008.
[19] H. Koo *et al.*, ‘In vivo targeted delivery of nanoparticles for theranosis’, *Acc. Chem. Res.*, vol. 44, no. 10, pp. 1018–1028, Oct. 2011.

[20] F. K. Swirski *et al.*, ‘Identification of splenic reservoir monocytes and their deployment to inflammatory sites’, *Science*, vol. 325, no. 5940, pp. 612–616, Jul. 2009.
[21] M. M. de Villiers, P. Aramwit, and G. S. Kwon, Eds., *Nanotechnology in Drug Delivery*. New York: Springer-Verlag, 2009.
[22] T. Schluep *et al.*, ‘Pharmacokinetics and tumor dynamics of the nanoparticle IT-101 from PET imaging and tumor histological measurements’, *Proc. Natl. Acad. Sci.*, vol. 106, no. 27, pp. 11394–11399, Jul. 2009.
[23] H. J. Johnston, M. Semmler-Behnke, D. M. Brown, W. Kreyling, L. Tran, and V. Stone, ‘Evaluating the uptake and intracellular fate of polystyrene nanoparticles by primary and hepatocyte cell lines in vitro’, *Toxicol. Appl. Pharmacol.*, vol. 242, no. 1, pp. 66–78, Jan. 2010.
[24] Z. Chen *et al.*, ‘Bio-distribution and metabolic paths of silica coated CdSeS quantum dots’, *Toxicol. Appl. Pharmacol.*, vol. 230, no. 3, pp. 364–371, Aug. 2008.
[25] M. Hamidi, A. Azadi, and P. Rafiei, ‘Pharmacokinetic consequences of pegylation’, *Drug Deliv.*, vol. 13, no. 6, pp. 399–409, Dec. 2006.
[26] M. Ohlson, J. Sörensson, and B. Haraldsson, ‘A gel-membrane model of glomerular charge and size selectivity in series’, *Am. J. Physiol. Renal Physiol.*, vol. 280, no. 3, pp. F396-405, Mar. 2001.
[27] W. M. Deen, M. J. Lazzara, and B. D. Myers, ‘Structural determinants of glomerular permeability’, *Am. J. Physiol. Renal Physiol.*, vol. 281, no. 4, pp. F579-596, Oct. 2001.
[28] C. H. J. Choi, J. E. Zuckerman, P. Webster, and M. E. Davis, ‘Targeting kidney mesangium by nanoparticles of defined size’, *Proc. Natl. Acad. Sci. U. S. A.*, vol. 108, no. 16, pp. 6656–6661, Apr. 2011.
[29] J. R. Lakowicz, *Principles of Fluorescence Spectroscopy*, 3rd ed. Springer US, 2006.
[30] S. Gregersen, T. Vosch, and K. J. Jensen, ‘Peptide-Stabilized, Fluorescent Silver Nanoclusters: Solid-Phase Synthesis and Screening’, *Chem. – Eur. J.*, vol. 22, no. 51, pp. 18492–18500, 2016.
[31] J. C. Stockert and A. Blázquez-Castro, *Fluorescence Microscopy in Life Sciences*. 2017.
[32] J. Pawley, Ed., *Handbook of Biological Confocal Microscopy*, 3rd ed. Springer US, 2006.
[33] ‘Methods in Cell Biology | Cell Biologcal Applications of Confocal Microscopy | ScienceDirect.com’. [Online]. Available: https://www.sciencedirect.com/bookseries/methods-in-cell-biology/vol/38. [Accessed: 05-Aug-2019].
[34] M. Dailey, G. Marrs, J. Satz, and M. Waite, ‘Concepts in Imaging and Microscopy: Exploring Biological Structure and Function with Confocal Microscopy’, *Biol. Bull.*, vol. 197, no. 2, pp. 115–122, 1999.
[35] R. A. Malik *et al.*, ‘Corneal confocal microscopy: a non-invasive surrogate of nerve fibre damage and repair in diabetic patients’, *Diabetologia*, vol. 46, no. 5, pp. 683–688, May 2003.
[36] N. Chen, G. Gao, and S. P. Chong, ‘Focal Modulation Microscopy: Principle and Techniques’, *Mol. Imaging*, Mar. 2012.
[37] K. Svoboda and S. M. Block, ‘Biological applications of optical forces’, *Annu. Rev. Biophys. Biomol. Struct.*, vol. 23, pp. 247–285, 1994.
[38] ‘Functional Clustering Drives Encoding Improvement in a Developing Brain Network during Awake Visual Learning’. [Online]. Available: https://journals.plos.org/plosbiology/article?id=10.1371/journal.pbio.1001236. [Accessed: 05-Aug-2019].
[39] ‘Measurement of pH Values in Human Tissues by Two-Photon Microscopy - Park - 2012 -

Angewandte Chemie International Edition - Wiley Online Library'. [Online]. Available: https://onlinelibrary.wiley.com/doi/abs/10.1002/anie.201109052. [Accessed: 05-Aug-2019].
[40] D. Rendell, D. J. Mowthorpe, and ACOL (Project), *Fluorescence and phosphorescence spectroscopy*. Published on behalf of ACOL, London by Wiley, 1987.
[41] Gauglitz, G. V.-D. Gauglitz, and T. Vo-Dinh, *Handbook of Spectroscopy*. 2003.
[42] C. Pautke *et al.*, 'Tetracycline bone fluorescence: a valuable marker for osteonecrosis characterization and therapy', *J. Oral Maxillofac. Surg. Off. J. Am. Assoc. Oral Maxillofac. Surg.*, vol. 68, no. 1, pp. 125–129, Jan. 2010.
[43] F. Wang, W. B. Tan, Y. Zhang, X. Fan, and M. Wang, 'Luminescent nanomaterials for biological labelling', *Nanotechnology*, vol. 17, no. 1, pp. R1–R13, Nov. 2005.
[44] S. C. Hung, J. Ju, R. A. Mathies, and A. N. Glazer, 'Energy transfer primers with 5- or 6-carboxyrhodamine-6G as acceptor chromophores', *Anal. Biochem.*, vol. 238, no. 2, pp. 165–170, Jul. 1996.
[45] K. L. Holmes and L. M. Lantz, 'Protein labeling with fluorescent probes', *Methods Cell Biol.*, vol. 63, pp. 185–204, 2001.
[46] L. G. Lee, C. H. Chen, and L. A. Chiu, 'Thiazole orange: a new dye for reticulocyte analysis', *Cytometry*, vol. 7, no. 6, pp. 508–517, Nov. 1986.
[47] G. Patonay, J. Salon, J. Sowell, and L. Strekowski, 'Noncovalent labeling of biomolecules with red and near- infrared dyes', *Mol. Basel Switz.*, vol. 9, no. 3, pp. 40–49, Feb. 2004.
[48] A. Mishra, R. K. Behera, P. K. Behera, B. K. Mishra, and G. B. Behera, 'Cyanines during the 1990s: A Review', *Chem. Rev.*, vol. 100, no. 6, pp. 1973–2012, Jun. 2000.
[49] A. A. Ishchenko, N. A. Derevyanko, and V. A. Svidro, 'Effect of the polymethine chain length on the fluorescence spectrum of symmetric cyanine dyes', *Opt. Spectrosc. - OPT SPECTROSC*, vol. 72, pp. 60–62, Jan. 1992.
[50] R. B. Mujumdar, L. A. Ernst, S. R. Mujumdar, C. J. Lewis, and A. S. Waggoner, 'Cyanine dye labeling reagents: Sulfoindocyanine succinimidyl esters', *Bioconjug. Chem.*, vol. 4, no. 2, pp. 105–111, Mar. 1993.
[51] S. Mahmudi-Azer, P. Lacy, B. Bablitz, and R. Moqbel, 'Inhibition of nonspecific binding of fluorescent-labelled antibodies to human eosinophils', *J. Immunol. Methods*, vol. 217, no. 1–2, pp. 113–119, Aug. 1998.
[52] R. Heim, D. C. Prasher, and R. Y. Tsien, 'Wavelength mutations and posttranslational autoxidation of green fluorescent protein', *Proc. Natl. Acad. Sci. U. S. A.*, vol. 91, no. 26, pp. 12501–12504, Dec. 1994.
[53] '(PDF) Luminescent nanomaterials for biological labeling'. [Online]. Available: https://www.researchgate.net/publication/231059373_Luminescent_nanomaterials_for_biological_labeling. [Accessed: 05-Aug-2019].
[54] Y. G. Yanushevich *et al.*, 'A strategy for the generation of non-aggregating mutants of Anthozoa fluorescent proteins', *FEBS Lett.*, vol. 511, no. 1–3, pp. 11–14, Jan. 2002.
[55] 'Lanthanide Luminescence for Biomedical Analyses and Imaging | Chemical Reviews'. [Online]. Available: https://pubs.acs.org/doi/10.1021/cr900362e. [Accessed: 05-Aug-2019].
[56] J.-C. G. Bünzli, 'Lanthanide luminescence for biomedical analyses and imaging', *Chem. Rev.*, vol. 110, no. 5, pp. 2729–2755, May 2010.
[57] 'Synthesis of a Terbium Fluorescent Chelate and Its Application to Time-Resolved Fluoroimmunoassay | Analytical Chemistry'. [Online]. Available: https://pubs.acs.org/doi/abs/10.1021/ac0013305. [Accessed: 05-Aug-2019].
[58] M. Bruchez, M. Moronne, P. Gin, S. Weiss, and A. P. Alivisatos, 'Semiconductor Nanocrystals as Fluorescent Biological Labels', *Science*, vol. 281, no. 5385, pp. 2013–2016, 1998.

[59] X. Michalet *et al.*, ‘Quantum dots for live cells, in vivo imaging, and diagnostics’, *Science*, vol. 307, no. 5709, pp. 538–544, Jan. 2005.
[60] E. Fleige, M. A. Quadir, and R. Haag, ‘Stimuli-responsive polymeric nanocarriers for the controlled transport of active compounds: concepts and applications’, *Adv. Drug Deliv. Rev.*, vol. 64, no. 9, pp. 866–884, Jun. 2012.
[61] S. Ganta, H. Devalapally, A. Shahiwala, and M. Amiji, ‘A review of stimuli-responsive nanocarriers for drug and gene delivery’, *J. Control. Release Off. J. Control. Release Soc.*, vol. 126, no. 3, pp. 187–204, Mar. 2008.
[62] M. Calderón, M. A. Quadir, M. Strumia, and R. Haag, ‘Functional dendritic polymer architectures as stimuli-responsive nanocarriers’, *Biochimie*, vol. 92, no. 9, pp. 1242–1251, Sep. 2010.
[63] P. Vaupel, F. Kallinowski, and P. Okunieff, ‘Blood flow, oxygen and nutrient supply, and metabolic microenvironment of human tumors: a review’, *Cancer Res.*, vol. 49, no. 23, pp. 6449–6465, Dec. 1989.
[64] K. Ulbrich, T. Etrych, P. Chytil, M. Jelínková, and B. Říhová, ‘Antibody-targeted polymer-doxorubicin conjugates with pH-controlled activation’, *J. Drug Target.*, vol. 12, no. 8, pp. 477–489, 2004.
[65] P. M. Loadman, M. C. Bibby, J. A. Double, W. M. Al-Shakhaa, and R. Duncan, ‘Pharmacokinetics of PK1 and Doxorubicin in Experimental Colon Tumor Models with Differing Responses to PK1’, *Clin. Cancer Res.*, vol. 5, no. 11, pp. 3682–3688, Nov. 1999.
[66] S. Matsumoto *et al.*, ‘Environment-responsive block copolymer micelles with a disulfide cross-linked core for enhanced siRNA delivery’, *Biomacromolecules*, vol. 10, no. 1, pp. 119–127, Jan. 2009.
[67] J. C. Cuggino *et al.*, ‘Thermosensitive nanogels based on dendritic polyglycerol and N-isopropylacrylamide for biomedical applications’, *Soft Matter*, vol. 7, no. 23, pp. 11259–11266, Nov. 2011.
[68] C. Kojima, S. Tsumura, A. Harada, and K. Kono, ‘A collagen-mimic dendrimer capable of controlled release’, *J. Am. Chem. Soc.*, vol. 131, no. 17, pp. 6052–6053, May 2009.
[69] T. D. Clemons, R. Singh, A. Sorolla, N. Chaudhari, A. Hubbard, and K. S. Iyer, ‘Distinction Between Active and Passive Targeting of Nanoparticles Dictate Their Overall Therapeutic Efficacy’, *Langmuir ACS J. Surf. Colloids*, vol. 34, no. 50, pp. 15343–15349, 18 2018.
[70] D. Wang, T. Zhao, X. Zhu, D. Yan, and W. Wang, ‘Bioapplications of hyperbranched polymers’, *Chem. Soc. Rev.*, vol. 44, no. 12, pp. 4023–4071, Jun. 2015.
[71] D. O. Kuethe, V. C. Behr, and S. Begay, ‘Volume of rat lungs measured throughout the respiratory cycle using 19F NMR of the inert gas SF6’, *Magn. Reson. Med.*, vol. 48, no. 3, pp. 547–549, Sep. 2002.
[72] L. M. G. de Araújo, L. C. Serigiolle, H. M. P. Gomes, D. A. B. Rodrigues, C. M. Lopes, and P. L. S. Leme, ‘Volume calculation of rats’ organs and its application in the validation of the volume relation between the abdominal cavity and the hernial sac in incisional hernias with “loss of abdominal domain”’, *Arq. Bras. Cir. Dig. ABCD Braz. Arch. Dig. Surg.*, vol. 27, no. 3, pp. 177–181, Sep. 2014.
[73] K. Krishnan and T. Peyret, ‘Physiologically Based Toxicokinetic (PBTK) Modeling in Ecotoxicology’, in *Ecotoxicology Modeling*, vol. 2, J. Devillers, Ed. Boston, MA: Springer US, 2009, pp. 145–175.
[74] L. Tang, A. M. Persky, G. Hochhaus, and B. Meibohm, ‘Pharmacokinetic aspects of biotechnology products’, *J. Pharm. Sci.*, vol. 93, no. 9, pp. 2184–2204, Sep. 2004.
[75] C. Oussoren, J. Zuidema, D. J. Crommelin, and G. Storm, ‘Lymphatic uptake and biodistribution of liposomes after subcutaneous injection. II. Influence of liposomal size,

lipid compostion and lipid dose', *Biochim. Biophys. Acta*, vol. 1328, no. 2, pp. 261–272, Sep. 1997.
[76] B. Meibohm and H. Zhou, 'Characterizing the impact of renal impairment on the clinical pharmacology of biologics', *J. Clin. Pharmacol.*, vol. 52, no. 1 Suppl, pp. 54S-62S, Jan. 2012.
[77] A. C. Croce and G. Bottiroli, 'Autofluorescence spectroscopy and imaging: a tool for biomedical research and diagnosis', *Eur. J. Histochem. EJH*, vol. 58, no. 4, p. 2461, Dec. 2014.
[78] J. B. Taylor and D. J. Triggle, *Comprehensive medicinal chemistry II*. Amsterdam; London: Elsevier, 2007.
[79] S. W. Paddock and K. W. Eliceiri, 'Laser scanning confocal microscopy: history, applications, and related optical sectioning techniques', *Methods Mol. Biol. Clifton NJ*, vol. 1075, pp. 9–47, 2014.
[80] M. Levitus and S. Ranjit, 'Cyanine dyes in biophysical research: the photophysics of polymethine fluorescent dyes in biomolecular environments', *Q. Rev. Biophys.*, vol. 44, no. 1, pp. 123–151, Feb. 2011.
[81] Y.-Z. Liu, Y.-X. Wang, and C.-L. Jiang, 'Inflammation: The Common Pathway of Stress-Related Diseases', *Front. Hum. Neurosci.*, vol. 11, p. 316, 2017.
[82] OECD, *Test No. 417: Toxicokinetics*. OECD, 2010.
[83] K. Mohr *et al.*, 'Aggregation Behavior of Polystyrene-Nanoparticles in Human Blood Serum and its Impact on the in vivo Distribution in Mice', *J. Nanomedicine Nanotechnol.*, vol. 05, Jan. 2014.
[84] 'Interaction of Nanoparticles With Biomolecules, Protein, Enzymes, and Its Applications', *Precis. Med.*, pp. 253–276, Jan. 2018.
[85] C. Neyen *et al.*, 'Macrophage scavenger receptor a promotes tumor progression in murine models of ovarian and pancreatic cancer', *J. Immunol. Baltim. Md 1950*, vol. 190, no. 7, pp. 3798–3805, Apr. 2013.
[86] M. Cataldi, C. Vigliotti, T. Mosca, M. Cammarota, and D. Capone, 'Emerging Role of the Spleen in the Pharmacokinetics of Monoclonal Antibodies, Nanoparticles and Exosomes', *Int. J. Mol. Sci.*, vol. 18, no. 6, Jun. 2017.
[87] R. Warrington, W. Watson, H. L. Kim, and F. R. Antonetti, 'An introduction to immunology and immunopathology', *Allergy Asthma Clin. Immunol. Off. J. Can. Soc. Allergy Clin. Immunol.*, vol. 7, no. Suppl 1, p. S1, Nov. 2011.
[88] Y. Deng *et al.*, 'The effect of hyperbranched polyglycerol coatings on drug delivery using degradable polymer nanoparticles', *Biomaterials*, vol. 35, no. 24, pp. 6595–6602, Aug. 2014.
[89] S. González-Rodríguez *et al.*, 'Polyglycerol-opioid conjugate produces analgesia devoid of side effects', *eLife*, vol. 6, 04 2017.